npj | computational materials

Article

Published in partnership with the Shanghai Institute of Ceramics of the Chinese Academy of Sciences

https://doi.org/10.1038/s41524-025-01795-z

Magnetoelectricity of topological solitons in 2D magnets

Alexander Edström[1,2] ✉, Paolo Barone[3] ✉, Silvia Picozzi[4,5] & Massimiliano Stengel[6,7]

We develop a multiscale approach to magnetoelectric effects, bridging atomistic and continuum models, with all parameters determined from ab initio electronic structure calculations. We show that the parameters of the model are equivalent to the electric field-induced Dzyaloshinski-Moriya interactions. After careful validation, we apply the models to study electric polarization and dipole moments carried by spin spirals and topological solitons, in the form of magnetic domain walls and Skyrmions, in the prototypical 2D magnet CrI_3. We show that the reduced symmetry of the material leads to additional magnetoelectric coupling terms, dominating over those expected in high symmetry (cubic) materials. An interesting consequence is that Skyrmions carry an out-of-plane electric dipole moment, while that of anti-Skyrmions is an order of magnitude larger and in-plane. Finally, we discuss the possibility to stabilize non-collinear spin states using electric fields.

The linear magnetoelectric effect, manifesting itself as a bilinear coupling between magnetization and electric polarization, was first predicted[1] and observed[2] in Cr_2O_3. Later, a range of magnetoelectric effects describing the coupling between magnetic and electric order parameters has been investigated, including inhomogeneous ones[3], where a spatially varying magnetic order induces an electric polarization. This effect has been widely studied in the field of multiferroics[4,5], where an electric polarization is induced by spin spiral states in so-called type II multiferroics[6,7]. Conversely, applied electric fields and the resulting electric polarization induce Dzyaloshinskii-Moriya interactions[8], which stabilize non-collinear spin textures in otherwise collinear ferromagnets. Due to the same mechanisms, other inversion symmetry-breaking magnetic structures can also generate an electric polarization, coupling them to electric fields. For example, topological solitons, such as magnetic domain walls (DWs)[9], which separate regions with different orientations of magnetization, can carry an electric dipole moment[6]. Magnetic DWs are technologically interesting as functional units, e.g., for racetrack memories[10], and the possibility of controlling them by electrical means is attractive in this context. Also, Skyrmions[11,12], another form of topologically protected magnetic soliton with widespread interest, can carry a local polarization and net electric dipole moment. While many of the early Skyrmion materials studied were metallic, recent examples include insulating ones where an electric polarization has been observed[13,14]. This finding enabled electric field control of Skyrmions[15], inspiring further efforts to stabilize Skyrmions with electric fields[16–19], even in antiferromagnets (AFMs)[20]. Topological magnetic solitons, such as DWs or Skyrmions, are spatially localized but extend over length scales of at least several nanometers or more, leaving them beyond the reach of direct first principles calculations, and hampering a thorough theoretical understanding and efficient design of functional materials. A few earlier works made theoretical estimates of the polarization of atomically sharp magnetic DWs, via a magnetostrictive mechanism[21–24], neglecting spin-orbit coupling (SOC). Such a description is of limited use for DWs in real materials, which can span up to hundreds of nanometers. A more sophisticated treatment calls for multiscale methods enabling an accurate description of magnetoelectric effects at different length scales, with realistic, materials-specific parameters, determined from first principles, electronic structure calculations. Such studies have recently appeared in the literature, using complex magnetoelectric models that often lack careful and systematic validation. In some cases, the studies show conspicuous discrepancies, as is the case, for example, for the 2D magnet CrI_3[17,25,26].

Since the discovery of long-range magnetic order in 2D monolayers of Van Der Waals materials, such as CrI_3[27–30], massive research efforts have led to exciting developments, including experimental realization of 2D monolayer magnets exhibiting multiferroicity[31] and Skyrmions[32]. These ultrathin magnets are interesting in the context of magnetoelectric effects; a moderate voltage is sufficient to produce a huge electric field in the perpendicular direction, and even metallic magnets may be possibly manipulated using such fields when the penetration length exceeds the thickness. Moreover, their high flexibility and tendency to ripple raise a number of fundamental questions about the possible interplay of magnetoelectric effects and layer curvature. The recent surge of interest in flexoelectricity (i.e., the linear coupling between strain gradients and electric polarization[33–35]) and

[1]Department of Applied Physics, KTH Royal Institute of Technology, Stockholm, Sweden. [2]Wallenberg Initiative Materials Science for Sustainability (WISE), KTH Royal Institute of Technology, Stockholm, Sweden. [3]Consiglio Nazionale delle Ricerche CNR-SPIN, Rome, Italy. [4]Department of Materials Science, University of Milan-Bicocca, Milan, Italy. [5]Consiglio Nazionale delle Ricerche CNR-SPIN, Chieti, Italy. [6]Institut de Ciència de Materials de Barcelona (ICMAB-CSIC), Bellaterra, Spain. [7]ICREA - Institució Catalana de Recerca i Estudis Avançats, Barcelona, Spain. ✉e-mail: aleeds@kth.se; paolo.barone@spin.cnr.it

flexomagnetism (defined as a modification of the spin parameters due to curvature[36]) thus provides additional motivation to explore magnetoelectric effects in the same materials, especially in 2D magnets such as CrI_3[37]. And indeed, recent works have revealed intriguing similarities between the phenomenology of applied electric fields and flexural deformations: for example, both lead to the appearance of an induced Dzyaloshinskii-Moriya interaction (DMI)[26,38–40], which is a universal feature of systems with broken space inversion symmetry[41,42], and an important ingredient in the stabilization of topological structures.

Here, we develop a multiscale approach, described in "Methods," considering atomistic and continuum models of magnetoelectricity, with all parameters determined using first principles density functional theory (DFT) calculations. We carefully validate these models against direct DFT calculations of other complex spin states that differ from those used to build the model. We also show how the magnetoelectric coupling parameters correspond precisely to the linear terms of the electric field-induced DMI, in both the atomistic and continuum forms. Next, we apply the models to study the electric polarization of spin spirals and magnetic topological solitons in the form of DWs and Skyrmions, and assess the possibility of magnetoelectric engineering of these topological solitons. Interestingly, while most studies of electric field effects on 2D magnetism have focused on perpendicular electric fields[17,19]. We find that the magnetoelectric coupling in CrI_3 is more than an order of magnitude stronger for in-plane electric fields. The continuum model provides a particularly simple description in terms of only three parameters, giving useful insights into the magnetoelectric phenomena, for example showing that Skyrmions carry out-of-plane electric dipole moments, while anti-Skyrmions carry in-plane dipole moments.

Results

Early discussions of the electric polarization induced by non-collinear spin configurations and spin spirals include phenomenological descriptions, as in earlier Ref. 3 or in Ref. 43, and microscopic mechanisms, such as the purely electronic one proposed by Katsura, Nagaosa, and Balatsky (KNB) relating spin currents and electric polarization[44]. The KNB model is essentially a dimer model comprising two magnetic atoms in a cubic environment, predicting a polarization contribution in direction $\hat{\mathbf{e}}_{12}\times(\hat{\mathbf{e}}_1\times\hat{\mathbf{e}}_2)$ for two spins parallel to $\hat{\mathbf{e}}_1$ and $\hat{\mathbf{e}}_2$, respectively, and separated in the direction $\hat{\mathbf{e}}_{12}$. Despite its physical insight, the KNB result is limited to cases described by the model itself, which is a very specific one, failing, e.g., in describing the spin-driven ferroelectricity of triangular-lattice multiferroics of the delafossite family[45]. However, the underlying idea of decomposing spin-induced polarization in spin-dimer contributions has been later pursued[46,47], providing a generalization of the KNB model in the form of a pairwise, interatomic, coupling tensor. The latter has successfully described the electric polarization induced by complex spin textures in low-symmetry crystal classes[48–53], including 2D multiferroics[31]. This is the atomistic model, which we use and describe further in "Atomistic Model".

Considering a phenomenological continuum model in cubic symmetry, Mostovoy[43] found a similar result as Katsura et al., showing, for example, that a helix has zero polarization while a cycloid carries a polarization parallel to $\hat{\mathbf{e}}_3\times\mathbf{q}$, where $\hat{\mathbf{e}}_3$ is the spin rotation axis and $\mathbf{q}$ the propagation vector. Here, we adopt a more general continuum form of the inhomogeneous magnetoelectric effect, which was introduced by Baryakhtar et al.[3] without assuming a specific crystalline symmetry (see "Continuum Model").

In the following two sections, we introduce the atomistic and continuum models of magnetoelectricity used in this work, respectively, and determine their mutual connections. Next, we describe specifics of these models for monolayer CrI_3. We then present our calculated values, and validate them on representative spin structures that differ from those used to construct our model. Finally, we apply the models to magnetic DWs and Skyrmions.

Atomistic model

Within an atomistic approach, the macroscopic polarization is decomposed in atomic and pairwise contributions[46,47], as detailed in "Macroscopic polarization induced by spiral magnetism within the atomistic approach". In centrosymmetric systems, the magnetically induced polarization arising from non-collinearity of spins in a helimagnetic configuration takes the form of a generalized spin-current (gKNB) coupling:

$$\mathbf{P}=\frac{1}{2\Omega}\sum_{i,j}\mathcal{M}^{ij}(\mathbf{S}_i\times\mathbf{S}_j), \tag{1}$$

where Ω denotes the unit cell volume (area) in the 3D (2D) case, the i index denotes all lattice sites in the cell, j runs over all neighbors for each given site (typically restricted to a few nearest-neighbor shells), while the prefactor 1/2 is introduced to count each bond contribution only once. We consider normalized spins. Note the antisymmetric character of the interaction in the two participating spin components; indeed, it can be shown that only the cross product of the spins contributes to the macroscopic polarization induced by spiral magnets (see "Macroscopic polarization induced by spiral magnetism within the atomistic approach"). The 3 × 3 matrix $\mathcal{M}^{ij}$ generalizes the standard KNB result, describing the magnetoelectric (spin-dipole) coupling. In the most general case, it is uniquely determined by 9 coefficients for each bond. Crystalline symmetries introduce constraints on the form of the coupling tensor and its allowed nonzero coefficients, both in deriving the transformation rules relating $\mathcal{M}^{ij}$ of different symmetry-equivalent bonds and in determining its symmetry-allowed form for each bond, that will depend on the subset of symmetry operations of the bonding vector (Supplementary Note 1).

In a first-principles context, the magnetoelectric interaction matrix $\mathcal{M}^{ij}$ can be calculated following the procedure outlined in Ref. 47. In particular, each column of the matrix for a given pair of spins is evaluated from the linear combinations of polarizations calculated for a set of selected non-collinear spin-dimer states at fixed atomic positions. The last assumption implies that only the electronic contributions to the spin-induced polarization are taken into account, and they will be our exclusive focus in the following. However, the analysis can be generalized to include also the spin-order-induced ionic contribution to macroscopic polarization, following, e.g., Ref. 54. As mentioned above, the approach has been successfully applied to describe the spin-driven polarization of several low-symmetry materials, such as triangular lattice multiferroics[31,48–53].

The expression in Eq. (1) takes on a strikingly similar form to the atomistic Dzyaloshinskii-Moriya interaction (DMI). Comparing the electric dipole energy $E=\mathcal{E}\cdot\mathbf{p}$ of a homogeneous electric field $\mathcal{E}$ coupled to an electric dipole $\mathbf{p}$, we can immediately extract the electric field-induced DMIs. The DMI energy contribution of a pair of atomic spins is[42]

$$E_{ij}=\mathbf{D}^{ij}\cdot(\mathbf{S}_i\times\mathbf{S}_j), \tag{2}$$

while the electric dipole moment of the same spin pair is $\mathbf{p}_{ij}=\mathcal{M}^{ij}(\mathbf{S}_i\times\mathbf{S}_j)$, with energy $E_{ij}=-\mathcal{E}\cdot\mathbf{p}_{ij}$ Equating these expressions for E_{ij} gives the electric field induced by atomistic DMI

$$\mathbf{D}^{ij}(\mathcal{E})=-(\mathcal{M}^{ij})^T\mathcal{E}\quad\text{or}\quad\mathcal{M}^{ij}_{\alpha\beta}=-\frac{\partial D^{ij}_\beta}{\partial\mathcal{E}_\alpha}. \tag{3}$$

As shown in Supplementary Note 1, it is straightforward to check that Moriya's rules for the Dzyaloshinskii vector $\boldsymbol{D}(\mathcal{E})$ are easily recovered using the symmetry constraints on the local coupling tensor $\mathcal{M}$ and identifying the symmetry operations compatible with the applied field $\mathcal{E}$. Thus, the magnetoelectric coupling tensors are equivalent to the electric-field-induced DMIs, and can be used, for example, to simulate an applied electric field in atomistic spin dynamics simulations. Although a close connection between magnetoelectricity and DMI was pointed out already by Sergienko and Dagotto[8], to the best of our knowledge, the direct relation in Eq. (3) was overlooked in earlier works; we regard it as one of our main formal results.

Continuum Model

Baryakhtar et al.[3] introduced a phenomenological continuum description of the inhomogeneous magnetoelectric effect, where the *local* polarization is given by $P_\alpha = f_{\alpha\beta,\gamma\delta} M_\delta \partial_\beta M_\gamma$. ($\mathbf{M}$ is the ferromagnetic order parameter and ∂_β is a short-hand symbol for the derivative along the Cartesian coordinate r_β.) This is indeed the most general form of the coupling between an arbitrary (pseudo)vector field and $\mathbf{P}$[55]: it can be trivially generalized to the antiferromagnetic order parameter as well. Nevertheless, one can show via an integration by parts that only the antisymmetric components of the tensor in the Cartesian indices $\gamma\delta$ contribute to the macroscopic polarization[43]. To reflect this fact, we write

$$P_\alpha = \tilde{f}_{\alpha\beta,\gamma\delta}\left(M_\gamma \partial_\beta M_\delta - M_\delta \partial_\beta M_\gamma\right), \tag{4}$$

where we have introduced the anti-symmetric tensor $\tilde{f}_{\alpha\beta,\delta\gamma} = \frac{1}{2}(f_{\alpha\beta,\delta\gamma} - f_{\alpha\beta,\gamma\delta})$ (see Supplementary Note 2).

In the following, we show that $\tilde{f}$ is directly related to the coefficients of the atomistic model, and establish a closed formula that yields the former as a function of the latter. The values in $\tilde{f}_{\alpha\beta,\gamma\delta}$ have a clear physical interpretation as the linear part in q_β of the polarization component α, arising for a spin spiral propagating along Cartesian direction β, with the spins rotating in the plane spanned by Cartesian directions γ, δ. Considering Eq. (1) in the small-$\mathbf{q}$ limit, each type of spin spiral (there are three possible planes of rotation for spins, propagating along an arbitrary Cartesian direction), yields three conditions for any given component P_α, leading to the 27 (3D) or 18 (2D) conditions needed to fully determine $\tilde{f}_{\alpha\beta,\gamma\delta}$ in terms of $\mathcal{M}^{ij}$. These can be compactly written as

$$\tilde{f}_{\alpha\beta,\gamma\delta} = \frac{1}{\Omega}\sum_{i,j,\lambda} \epsilon_{\gamma\delta\lambda} r^{ij}_\beta \mathcal{M}^{ij}_{\alpha\lambda}, \tag{5}$$

where $\epsilon_{\alpha\beta\gamma}$ is the anti-symmetric tensor and r^{ij}_β is the component β of the vector $\mathbf{r}^{ij}$ connecting spins i and j.

Next, we show that the relation to the DMI energy also holds in the continuum case, where the DMI energy density is[56]

$$E = D_{\alpha\beta\gamma}\left(M_\alpha \frac{\partial M_\beta}{\partial r_\gamma} - M_\beta \frac{\partial M_\alpha}{\partial r_\gamma}\right). \tag{6}$$

$D_{\alpha\beta\gamma}$ vanishes identically in the presence of space-inversion (SI) symmetry, but an external electric field breaks SI and allows for a nonzero $\mathbf{D}$. Comparing the energy density in Eq. (6) with that of an electric field $\mathcal{E}$ coupled to the polarization in Eq. (4), we find

$$\tilde{f}_{\alpha\beta,\gamma\delta} = -\frac{\partial D_{\gamma\delta\beta}}{\partial \mathcal{E}_\alpha}. \tag{7}$$

This result is the continuum counterpart of Eq. (3), relating the microscopic DMI and the spin-polarization coupling coefficients, and allows the effect of electric fields to be studied in micromagnetic models of modulated spiral orders. As such, Eq. (5) can be considered an alternative form of the usual relation between the atomistic and continuum DMI terms, available e.g. in Ref. 56.

Monolayer CrI_3

Here we briefly summarize the crystal structure and general properties of the CrI_3 monolayer, which we analyze in the remainder of the work as an illustrative demonstration of our approach. Fig. 1 displays the crystal structure of monolayer CrI_3 with space-group symmetry $P\bar{3}1m$ and crystallographic point group D_{3d}, comprising inversion, threefold rotation/rotoreflection axis orthogonal to the monolayer, three twofold in-plane rotational axes, and three vertical mirrors highlighted by dashed and solid lines, respectively. Cr atoms occupy the 2*c* Wyckoff position, with local D_3 symmetry, the two Wyckoff partners being related by inversion symmetry. The lattice constant is a = 6.71 Å, corresponding to a Cr-Cr distance of $\frac{a}{\sqrt{3}} = 3.87$ Å. Monolayers have been experimentally exfoliated and ordered ferromagnetically, with out-of-plane magnetization, below 45 K[27]. The magnetism of a material with uniaxial anisotropy is described by an energy

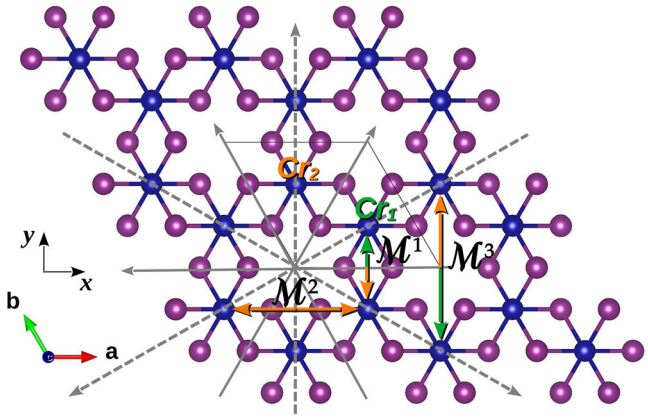

Fig. 1 | Crystal structure of the CrI_3 monolayer, highlighting the unit cell, the adopted Cartesian reference frame as well as symmetry axes and planes. Dashed lines represent the in-plane twofold rotation axes, solid lines the vertical mirror planes. The threefold rotation/rotoreflection axis is perpendicular to the monolayer plane. Inversion-partner Cr sites are highlighted within the unit cell. Two-headed arrows show the 1st, 2nd and 3rd NN bonds whose coupling tensors $\mathcal{M}_i$ have been evaluated; the presence of an inversion center in the bond is highlighted by bicolored arrows.

$$E = A\int\left([\nabla \mathbf{M}]^2 - \frac{1}{\xi^2}M_z^2\right)d^2r \tag{8}$$

with energy scale given by the spin stiffness A, and characteristic length scale $\xi = \sqrt{\frac{A}{K}}$, where K is the magnetic anisotropy. The 1st nearest-neighbor (NN) Cr-Cr bond has an inversion center whereby the corresponding interatomic DMI is zero, just like the continuum DMI, while the 2nd NN bond, which lacks an inversion center, has a DMI of around 60 μeV [57] with an associated appearance of topological magnons[58]. (See Fig. 1 for an illustration of the bonds.)

By taking into account the above symmetries, the magnetoelectric tensors associated with the bonds displayed in Fig. 1 take the form (see Supplementary Note 1 for details)

$$\mathcal{M}^1 = \begin{bmatrix} \mathcal{M}^1_{11} & 0 & \mathcal{M}^1_{13} \\ 0 & \mathcal{M}^1_{22} & 0 \\ \mathcal{M}^1_{31} & 0 & \mathcal{M}^1_{33} \end{bmatrix}, \tag{9}$$

$$\mathcal{M}^2 = \begin{bmatrix} 0 & \mathcal{M}^{12}_2 & 0 \\ \mathcal{M}^2_{21} & 0 & \mathcal{M}^2_{23} \\ 0 & \mathcal{M}^2_{32} & 0 \end{bmatrix}. \tag{10}$$

The 3rd NN tensor $\mathcal{M}^3$ takes the same form as $\mathcal{M}^1$. In principle, the local site- and bond-symmetries of CrI_3 would allow for additional (symmetric) intra- and inter-site contributions to $\mathbf{P}$ (see Appendices A,B). Besides being numerically small, these terms do not contribute to the macroscopic electric polarization of spin spirals nor general spatially slowly varying spin textures, and they will be neglected in the following.

As described in Supplementary Note 2, the most general tensor of the continuum model $f_{ik,\alpha\beta}$ is reduced to have 9 independent non-zero components in a CrI_3 monolayer, but only three remain in the anti-symmetric part, $\tilde{f}_{12,12}$, $\tilde{f}_{11,31}$ and $\tilde{f}_{31,31}$. The component $\tilde{f}_{12,12}$ corresponds to the in-plane polarization of a cycloid with spins in the plane, and is mainly important in systems with in-plane magnetization ($K < 0$), while it will be of

less importance in CrI_3 with perpendicular magnetization $K > 0$. The other two components, which we label $\tilde{f}_{ip} \equiv \tilde{f}_{11,31}$ and $\tilde{f}_z \equiv \tilde{f}_{31,31}$, correspond to the in-plane and out-of-plane components of polarization for a cycloid with out-of-plane spins. In high symmetry materials (point groups O_h, T_d and O, see Supplementary Note 2), $\tilde{f}_{ip} = 0$ while $\tilde{f}_z$ and $\tilde{f}_{12,12}$ are equal and non-zero, as in the model studied by Mostovoy[43], consistent with the KNB model[44]. The KNB model corresponds to the only non-zero elements of $\mathcal{M}^{ij}_{\alpha\beta}$ being $\mathcal{M}^1_{31} = -\mathcal{M}^1_{13}$, $\mathcal{M}^2_{32} = -\mathcal{M}^2_{23}$ and $\mathcal{M}^3_{31} = -\mathcal{M}^3_{13}$, that is precisely those which determine $\tilde{f}_z$ and $\tilde{f}_{12,12}$, which would be equal under such conditions (see Eqs. (15), (16)). The polarization due to $\tilde{f}_{ip}$ can be considered a magnetoelectric analog to the unconventional, in-plane flexoelectric response studied by Springolo et al.[35]. Note, however, that while the flexoelectric tensor is also a fourth rank tensor, but symmetric in the last two indices. The magnetoelectric response, which we focus on here, instead is given by a rank four tensor which is anti-symmetric in the last two indices.

Results for the calculated physical constants

The magnetic parameters of Eq. (8) are taken from an earlier calculation on the same material[37], where we found $K = 0.75$ meV/Cr and $A = 48$ meVÅ^2/Cr, corresponding to $\xi = \sqrt{A/K} = 8$ Å.

We calculated $\mathcal{M}^{ij}$ up to the fourth nearest neighbor (NN), following the procedure outlined in Ref. 47. The 2nd NN needs special care as the bond lacks an inversion center, leading to non-zero symmetric elements. Hence, the full intersite tensor (Eq. (29)) needs to be calculated and anti-symmetrized. The values for 1st, 2nd and 3rd NNs are (in units of 10^{-5} eÅ)

$$\mathcal{M}^1 = \begin{bmatrix} -79 & 0 & -98 \\ 0 & -20 & 0 \\ -59 & 0 & 6 \end{bmatrix} \tag{11}$$

$$\mathcal{M}^2 = \begin{bmatrix} 0 & 273 & 0 \\ 61 & 0 & 112 \\ 0 & 11 & 0 \end{bmatrix} \tag{12}$$

$$\mathcal{M}^3 = \begin{bmatrix} 109 & 0 & -33 \\ 0 & 55 & 0 \\ 0 & 0 & 0 \end{bmatrix}. \tag{13}$$

Some of the elements that are zero by symmetry numerically come out as order of magnitude $1 \cdot 10^{-5}$ eÅ, indicating the numerical accuracy of the calculations. The 4th NN is smaller than the former three, with its largest element being $17 \cdot 10^{-5}$ eÅ, and is neglected in the following. $\mathcal{M}^2$ has larger components than $\mathcal{M}^1$ and additionally has a higher coordination of six, compared to three for $\mathcal{M}^1$. Consequently, we expect $\mathcal{M}^2$ to be more important than $\mathcal{M}^1$ in describing the magnetoelectric polarization in CrI_3. Interestingly, the 3rd NN magnetoelectric interaction tensor $\mathcal{M}^3$ also has larger elements than those of $\mathcal{M}^1$. Thus, all of three NN interactions can be important, and as will be seen in the next section, including the three NN ME tensors is necessary and sufficient to accurately describe a variety of complex spin structures. We also determined the intrasite tensor (first term of Eq. (28)) and symmetric intersite part for the 2nd NN, and confirmed these also to be small compared to Eqs. (11)–(13). Thanks to the global space inversion (SI) symmetry of the crystal, neither of the latter would contribute to the macroscopic polarization induced by helimagnetic ordering.

Next, the parameters of the continuum model are determined from those of the discrete model, using the relations from Eq. (5), as listed below.

$$\tilde{f}_{ip} \equiv \tilde{f}_{11,31} = \tfrac{1}{a}\left(\mathcal{M}^1_{22} - \mathcal{M}^1_{11} + 2\sqrt{3}(\mathcal{M}^2_{21} + \mathcal{M}^2_{12}) + 2(\mathcal{M}^3_{11} - \mathcal{M}^3_{22})\right) = 198 \cdot 10^{-5} e \tag{14}$$

$$\tilde{f}_z \equiv \tilde{f}_{31,31} = \frac{2}{a}\left(\mathcal{M}^1_{31} + 2\sqrt{3}\mathcal{M}^2_{32} - 2\mathcal{M}^3_{31}\right) = -8 \cdot 10^{-5} e \tag{15}$$

$$\tilde{f}_{12,12} = -\frac{2}{a}\left(\mathcal{M}^1_{13} + 2\sqrt{3}\mathcal{M}^2_{23} - 2\mathcal{M}^3_{13}\right) = -106 \cdot 10^{-5} e \tag{16}$$

Given the relations in Eqs. (3) and (7), the numerical values listed above are the linear coefficients for the electric field-induced DMI. The DMI induced by finite electric fields has been calculated from first principles for monolayer CrI_3 in several works[17,25,26,59]. There are, however, discussions[17,25] and notable discrepancies between the data available in the literature. In particular, calculations in the generalized gradient approximation (GGA) produce results varying over 2 orders of magnitude and sign[17,26,59]. Meanwhile, our result for the 1st NN DMI, $D^1_z/\mathcal{E}_z = -\mathcal{M}^1_{33} = -6 \cdot 10^{-5}$ eÅ is in reasonable agreement with the LDA calculation of Ghosh et al.[25] giving a value of $D^1_z/\mathcal{E}_z = -13.5 \cdot 10^{-5}$ eÅ, even though our respective approaches differ: while Ghosh et al. calculated the DMI from energy differences under a finite electric field, and under the assumption that further neighbor DMI is negligible, while we calculated electric polarizations arising from non-collinear spin arrangements.

Earlier works have often focused on the out-of-plane DMI component D_z for a perpendicular electric field $\mathcal{E}_z$ and the first nearest neighbor bond[17,25,59]. Hence, it is also interesting to note that the component $\mathcal{M}^1_{33}$, which this corresponds to in the magnetoelectric interaction tensors, is relatively small. In fact, in-plane electric fields will be much more effective in inducing DMI, and as we have seen, 2nd and 3rd NN interactions are at least as, or more important than the first one. Finally, we point out that as the magnetoelectric tensors provide a complete description of the DMI induced by an arbitrary electric field, they provide an excellent starting point for further studies of electric field effects on magnetism, e.g., using atomistic spin dynamics simulations[60], allowing dynamics and finite temperatures to be investigated. To do that accurately, one should also include lattice-mediated effects, in addition to the electronic ones considered here. Ghosh et al.[25] argued that the effect of the electric field on the crystal structure is small, but the impact on the DMI parameters remains to be addressed. Ref. 25 also found a negligible effect of electric fields on A and K in CrI_3, using finite electric field calculations. This is expected since the effect of applied electric fields on these parameters is a higher (2nd) order effect, whereas only the DMI couples linearly to electric fields. Hence, in the following, we will treat A and K as independent of the applied electric field.

Recently, the curvature induced continuum DMI in CrI_3 was calculated to $\frac{D_{zyy}}{\kappa} = 3.3$ meV[37], compared to $\frac{D_{zyy}}{\mathcal{E}_z} = 181 \cdot 10^{-5}$ e found here. The ratio of these values is $\frac{\mathcal{E}_z}{\kappa} = 1.8$ V, which implies that an electric field of 1.8 mV/Å induces a similar DMI as a curvature of 10^{-3} Å^{-1}. In Ref 37 we predicted that a curvature of 0.07 Å^{-1} stabilizes a spin cycloid with lower energy than the FM state. In the following, we will find the analogous result of electric field-induced spin cycloids with a consistent order of magnitude of the critical field.

Validation

To validate the gKNB model and its computed parameters, we compare the predictions of the model to direct DFT calculations of the electric polarization for a representative non-collinear spin structure that differs from those used to numerically determine $\mathcal{M}^{ij}$. In particular, we consider a tilt of the spins corresponding to a $q = 0$ optical magnon mode. This means that every spin is tilted by an angle $\pm\,\theta$ along some in-plane direction $\hat{s} = (\cos\alpha, \sin\alpha, 0)$, in such a way that the tilt angle alternates in sign between 1st NN sites. Figure 2 shows the resulting electric polarization as a function of tilt angle θ for two distinct choices of $\hat{s}$: in (a) $\hat{s} = (1, 0, 0)$ is aligned with the $\hat{x}$ Cartesian direction, while $\hat{s} = (0, 1, 0) = \hat{y}$ in (b). The solid lines, showing the results of the full atomistic model (Eq. (1)), are in excellent agreement with the reslts of direct DFT calculations (symbols). Conversely, by truncating the model to 1st interactions (dashed curves), we obtain a marked discrepancy, both in magnitude and sign, with the reference DFT data. (Clearly, since the 2nd NN spins always remain parallel, the

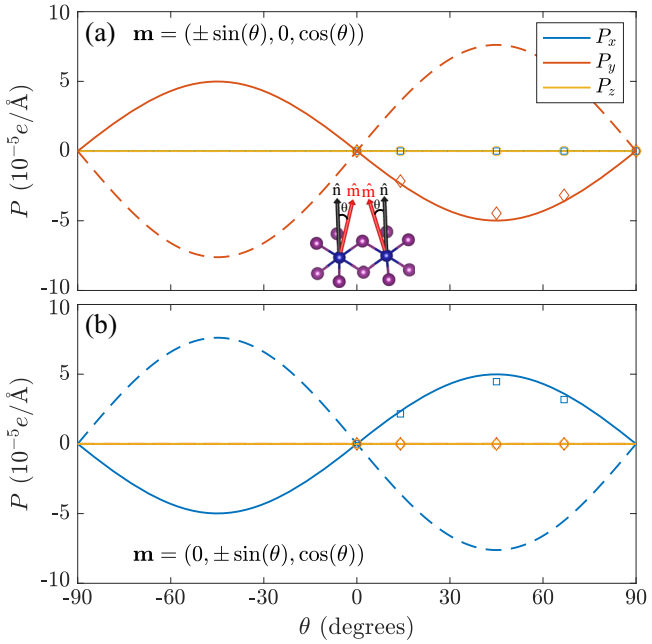

Fig. 2 | Electric polarization as a function of tilt angle θ, with neighboring Cr spins tilted in opposite x or y directions. a, **b** Electric polarization for spins tilted in the x or y directions, respectively. Markers show the result of direct DFT calculations, while the lines show the results of Eq. (1) using only 1st NN (dashed lines) or up to 3rd NN (solid lines) coupling.

matrix $\mathcal{M}_2$ does not contribute to the polarization.) This indicates that one should include at least up to 3rd NN interactions for a correct description of the ME coupling in CrI_3, and that the 3rd NN interaction is at least as important as the 1st NN one.

By comparing the two panels of Fig. 2, one can notice that the polarization is in both cases perpendicular to the canting direction $\hat{s}$, and has a sinusoidal dependence on the canting angle θ. In fact, as a consequence of the high symmetry of CrI_3, the electric dipole moment per Cr pair in the entire parameter space spanned by (α, θ) is determined by a single material constant via

$$\mathbf{p} = p_0 \sin 2\theta\ \hat{s}\times\hat{n}, \tag{17}$$

where $\hat{n}$ is the normal to the layer. The quantity $p_0 = \frac{3}{2}(M_1^{11} + M_1^{22} + M_3^{11} + M_3^{22}) = 98\cdot 10^{-5}$ eÅ describes the strength of the coupling between an electric field and an optical magnon, and can be regarded as a magnon analog to the Born effective charge of a phonon. The form of this dipole moment tells us that out-of-plane electric fields do not couple to the optical magnons, while in-plane electric fields do. As a consequence, an applied electric field will induce a non-zero anti-ferromagnetic (AFM) order parameter $\mathbf{L} = \frac{1}{2}(\mathbf{S}_1 - \mathbf{S}_2) = \sin\theta\hat{s}$, with $\mathbf{S}_1$ and $\mathbf{S}_2$ being neighboring spins. An in-plane electric field $\mathcal{E}$ leads to a tilt angle of $\tan 2\theta = \frac{2\mathcal{E}p_0}{J}$, where J = 11.6meV/Cr is the energy difference between the FM and AFM states. At small angles/electric fields, the AFM order parameter is proportional to the applied electric field, with 7 mV/Å resulting in an angle $\theta = 10°$ ($|\mathbf{L}| \approx 0.17$).

The data in Fig. 2 implies that if CrI_3 had Néel-type AFM order, a magnetization would be induced linearly with the applied electric field. In fact, it has been pointed out that $MnPS_3$, with the same crystallographic space group as CrI_3 but Néel type AFM order, is a linear magnetoelectric[61]. The calculations shown in Fig. 2 therefore illustrate how the model in Eq. (1) can also be used to calculate the homogeneous linear magnetoelectric effect, in addition to the inhomogeneous ones which are the main topic of this work.

Spin spirals

Next, we study the electric polarization of spin spirals. To define the structures, we use an orthogonal triad of unit vectors $\hat{s}$, $\hat{t}$ and $\hat{n}$ in such a way that $\hat{s} = \mathbf{q}/q = (\cos\alpha, \sin\alpha, 0)$ is the propagation direction ($\mathbf{q}$ is the wave vector of the spiral), $\hat{n}$ is the normal to the layer plane and $\hat{t} = \hat{n}\times\hat{s}$. We focus on two types of spirals, relevant in CrI_3: cycloids, rotating in the $t = 0$ plane, and helices, rotating in the $s = 0$ plane. The canting angle at a given magnetic site i is defined in all cases by $\theta_i = \mathbf{q}\cdot\mathbf{R}_i$. Figure 3 shows the electric polarization of cycloids (top) and helices (bottom), propagating in either x ($\alpha = 0$) or y-direction ($\alpha = \pi/2$). Again, the results of our full model (Eq. (1), solid curves) are in excellent agreement with the direct DFT calculations (symbols) of the polarization for the spin cycloids and helices, which we obtained by using supercells of length $L = \frac{2\pi}{q}$.

At difference with the case of the optical magnon, the 2nd NN interactions largely dominate the polarization of the spiral structures considered here, while the 1st and 3rd NN interactions have a comparatively smaller effect (except for P_z of the cycloids, where $\mathcal{M}_{31}^1$ gives a larger contribution than M_{32}^2 in Eq. (15)). This fact can be most clearly appreciated by looking at panels (b) and (d): The appearance of three maxima and three minima for the polarization on the interval $q_y \in [-\frac{2\pi}{d}, \frac{2\pi}{d}]$ is entirely due to the longer-range 2nd NN interactions, whereas the 1st NN interactions alone would have led to only two maxima and two minima on the same interval. Thus, our results again caution against using only the 1st NN interactions[47,54] in this class of physical problems, which may lead to a qualitatively incorrect description.

Remarkably, we find a large in-plane polarization for both helices and cycloids, while the out-of-plane components (only present in the latter) are comparatively much smaller. This outcome is in stark contrast with the predictions of the KNB spin current model[44]: According to the latter, the polarization of the cycloids should be parallel to $\hat{z}$, whereas that of the helices should be zero. The origin of the discrepancy is due to the assumption of cubic symmetry that is inherent to the KNB model. To see why in CrI_3 such an approach is not valid, it is useful to reason in terms of the continuum counterpart of our microscopic magnetoelectric model. As we mentioned in "Monolayer CrI3", $\tilde{f}_{\text{ip}} = \tilde{f}_{11,31}$ is symmetry-allowed in CrI_3, and this component is precisely the one responsible for the in-plane polarization of both helices and cycloids. (In fact, in the continuum limit, both helices and cycloids have the same in-plane component of polarization linear in q, and they only deviate at larger q.) The inappropriateness of KNB for noncubic crystal classes was evident already from experimental observations of electric polarization due the helical spin spirals[62], motivating the development of generalized models[47] such as Eq. (1). More recent examples also include spin cycloids with polarization components beyond the KNB model[63]. The symmetry based discussion and multiscale approach taken here is useful to understand which magnetoelectric effects can be expected depending on which crystal class and spin textures are involved. For example, in "Skyrmions: Polarization texture" we will see how the $\tilde{f}_{\text{ip}} = \tilde{f}_{11,31}$, which gives rise to the in-plane polarization of spin cycloids and helices, is precisely that which yields an in-plane polarization of anti-Skyrmions.

The electric polarization induced by non-collinear magnetic order, such as spin-spirals, has been extensively studied in the field of multiferroic materials, with experimentally measured polarization values ranging from $10^{-4}\mu$C/cm^2 in (Eu/Y)MnO_3 to 0.12μC/cm^2 in $DyMnO_3$[7,64]. This can be compared to the maximum values in Fig. 3, which correspond to 0.2μC/cm^2, well above what has previously been found in spin-spiral multiferroics, and it can be attributed to the strong SOC of I. Polarization values as large as 6.1μC/cm^2 have been theoretically predicted in the E-type AFM state of $HoMnO_3$[65,66], where, however, the microscopic origin of polarization has to be ascribed to Heisenberg exchange and not to the spin-orbit-driven "inverse-DMI" mechanism, as in the CrI_3 case.

Domain Walls: Structure and energetics

The above results for helical and cycloidal spin states confirm the accuracy of the 3rd NN atomistic model in describing the electric polarization of non-collinear magnetic textures in CrI_3, whereby the continuum model will, by construction, also accurately describe the polarization of these textures if the magnetization is slowly varying. Thus, we now have confidence to apply the models for calculating the electric polarization of other spin configurations,

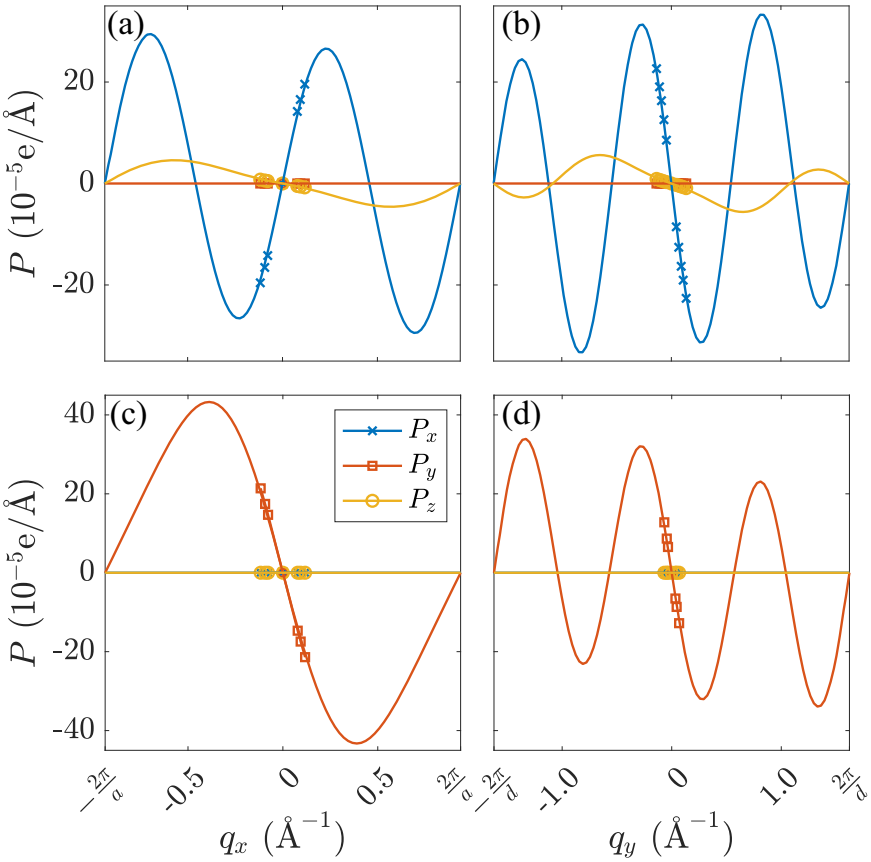

Fig. 3 | Electric polarization of spin spirals. Electric polarization as a function of spin cycloid (top **a**, **b**) or helix (bottom **c**, **d**) wavevector, for propagation in x (left **a**, **c**) or y-direction (right **b**, **d**), in a monolayer of CrI_3.

beyond the reach of direct DFT calculations, such as magnetic DWs. An isolated magnetic DW is characterized by rotation of the magnetization from $+\hat{z}$ to $-\hat{z}$ when moving along one direction $\hat{s} = (\cos\alpha, \sin\alpha, 0)$, parameterized by a coordinate $s = \mathbf{r} \cdot \hat{s}$, where the spins rotate in a plane normal to $\cos\beta\hat{t} - \sin\beta\hat{s}$. Then, $\beta = 0$ corresponds to a Néel-type DW and $\beta = \pi/2$ corresponds to a Bloch-type DW. Minimization of Eq. (8) for the corresponding boundary conditions gives a spin rotation profile with an angle $\theta(x) = 2\arctan(e^{x/\xi})$ between the out-of-plane direction $\hat{z}$ and the magnetization, where the DW width is determined by the length scale ξ and the DW energy is $E_{\mathrm{DW}} = 4\sqrt{AK} = 1.3$ meV/Å, with numerical values given for monolayer CrI_3[37]. Interestingly, adding a DMI term to the magnetic energy functional does not alter the form of the DW solution, although it does alter its relative energy.

For any magnetization that is periodic along one dimension $\mathbf{M}(0) = \mathbf{M}(L)$, there is an integer winding number

$$N = \frac{1}{2\pi}\int_0^L d\theta \tag{18}$$

where θ is the angle between the magnetization and its initial direction. A winding number N corresponds to a sequence of $2N$ DWs, but will also be identical for a spin spiral with wave number $q = \frac{2\pi}{L}$. In the coming section, we show that this winding number, together with the strength of the magnetoelectric coupling parameter, fully determines the net electric dipole moment per length.

Domain Walls: Electric polarization

From Eq. (4) a DW according to the description above has a polarization

$$\mathbf{P}(s) = \theta'(s)\left[\tilde{f}_{\mathrm{ip}}\cos(3\alpha+\beta)\hat{s} - \tilde{f}_{\mathrm{ip}}\sin(3\alpha+\beta)\hat{t} + \tilde{f}_z\cos\beta\hat{n}\right] \tag{19}$$

with a coordinate system such as that introduced in the previous section "Spin spirals". Given the rotational profile $\theta(s) = 2\arctan(e^{s/\xi})$ introduced above $\theta'(s) = \mathrm{sech}(s/\xi)/\xi$. The in-plane component of Eq. (19) clearly embodies the three-fold rotational symmetry of the CrI_3 crystal, in resemblance to the expression for flexoelectric polarization in Ref. 35. The solid curves in Fig. 4b–e show the resulting electric polarization profile in monolayer CrI_3, either for $\alpha = 0$ ($s = x$) or $\alpha = \pi/2$ ($s = y$), and for Néel or Bloch type DWs. The magnitude and direction of the polarization for the Néel or Bloch walls are similar to the cycloid and helix cases in Fig. 3, respectively, since the rotational sense of the spins is similar. Accordingly, the Néel wall polarization has the largest component along the $\hat{x}$-direction, with a small P_z, while the Bloch walls have $\mathbf{P} \parallel \hat{y}$. In both cases, the in-plane polarization changes sign if the DW is rotated by 90°. The maximum magnitude is also similar for the different cases, just below 10^{-5} eÅ. Converted into volume polarization using the I-layer distance as thickness, this corresponds to 0.1 μC/cm^2.

As a further test of our methodology, in all cases we recalculated the polarization profile by using Eq. (1) directly (we assume that the on-site values of the spins match the value of the continuum solution at the corresponding location); the results are plotted in Fig. 4b–e as dashed lines. While results agree reasonably well, there is a non-negligible discrepancy at the center of the DW, where the magnetization is varying most rapidly. This can be expected for a relatively thin DW, as the continuum model is only accurate for slowly varying magnetizations. We have confirmed (not shown) that by increasing ξ the agreement between the atomistic and continuum models becomes excellent, as it should for magnetizations varying slowly relative to the interatomic distance.

As previously pointed out by Mostovoy[43], another implication of the continuum model in Eq. (4) is that the net electric dipole moment over a DW depends on the rotation angle, while it is independent of DW profile and width. This can be anticipated from Eq. (19), where the s-dependence of the form $\theta'(s)$ is trivially integrated to $\int_{-\infty}^{\infty}\theta'(s)\mathrm{d}s = \pi$, so for e.g. $\beta = 0$ the

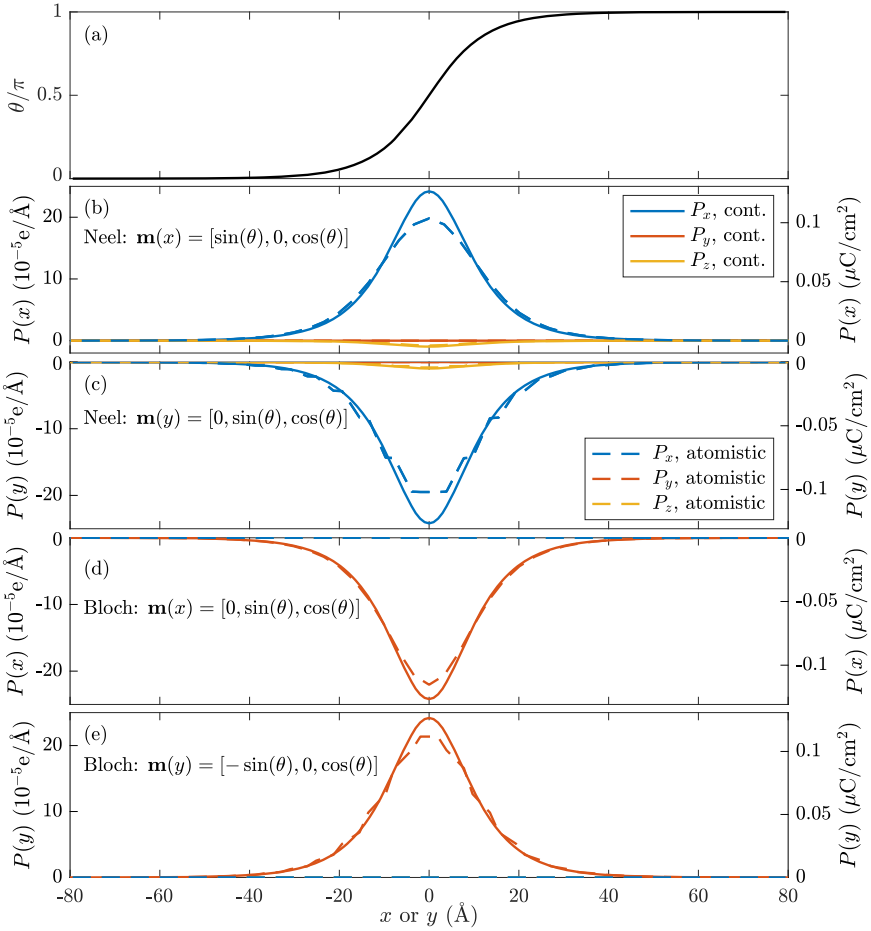

Fig. 4 | Electric polarization as a function of position for magnetic domain walls. a Spin rotation profile $\theta(s) = \arctan(e^{s/\xi})$ of a DW in CrI_3, with $\xi = 8$Å. **b–d** Electric polarization as a function of position along Bloch or Néel DWs, oriented along either x or y-direction, evaluated with either continuum (solid lines) or atomistic (dashed lines) model.

dipole moment per unit length is $\pi\left[\tilde{f}_{\rm ip}\cos(3\alpha)\hat{s} - \tilde{f}_{\rm ip}\sin(3\alpha)\hat{t} + \tilde{f}_z\hat{n}\right]$. This can be generalized to an arbitrary periodic spin texture with winding number given by Eq. (18). The net dipole moment per unit length of such a magnetization texture is proportional to N, depending only on the winding (and magnetoelectric parameters), not on the form of the function $\theta(x)$. Thus, the dipole moment of a DW is exactly half that of a spin spiral over one period. This holds in the continuum limit, where the spiral has a polarization which is linear in q, so that the polarization multiplied by the wavelength (the dipole moment per length) remains constant.

Domain Walls: Discussion

DWs bring in interesting new considerations in 2D monolayer magnets. While domain formation is ubiquitous in 3D bulk magnets, 2D monolayers with perpendicular anisotropy are persistently observed to form monodomains in experiments[67–70]. For example, in Fe_3GaTe_2 films, domain structure is observed down to thicknesses of 17.8 nm[71], below which a monodomain forms. This is consistent with simple arguments regarding magnetostatic dipole-dipole interactions in 2D vs 3D, as well as established theoretical results for domain formation in thin films with perpendicular magnetization; there exists a critical thickness under which magnetic films with perpendicular magnetic anisotropy only form monodomains[9,72,73]. For materials with strong perpendicular anisotropy, which is typically considered an important ingredient to overcome the Mermin-Wagner theorem and stabilize magnetic order in 2D magnets, a monodomain state is expected if the thickness is much smaller than $l_c = \frac{E_{\rm DW}}{2K_d}$, where $E_{\rm DW}$ is the DW energy and $K_d = \frac{1}{2}\mu_0 M_s^2$ the magnetic depolarizing field energy density for saturation magnetization M_s[9].

To see the reason, it is useful to observe that l_c coincides, modulo a dimensionless prefactor of the order of unity, with Kittel's length. In other words, Kittel's law would predict a domain periodicity of the order of $w = \sqrt{l_c d}$, where d is the thickness of the sample. If $l_c \gg d$, one obtains a value of w that is much larger than the film thickness, and the range of validity of Kittel's law breaks down. Indeed, in such a regime, the stray fields that are responsible for the magnetostatic energy cost are no longer confined to the surface but affect the whole volume of the film. For the same reason, spaced-apart DW's are hardly effective at reducing the depolarizing energy within the domains, and there is no driving force for their formation.

Considering material parameters for CrI_3[37], assuming an interlayer distance of $D = 7$ Å[27], one finds $l_c \approx 700D$, and a monolayer is clearly expected to form a single domain state. In practice, domains have been observed in samples as thin as 25 nm = $36D$[68]. Given that the DW energy is $E_{\rm DW} = 4\sqrt{AK}$, where A is the spin stiffness and K the magnetic anisotropy, and that a sizeable K is typically considered needed to stabilize magnetism in the 2D limit, domain formation in atomically thin samples would only be expected for extremely small values of A, i.e., if magnetism is entirely stabilized by anisotropy, with negligible exchange interactions. This raises the question of whether applied electric fields can be used to stabilize magnetic DWs in 2D monolayer magnets such as CrI_3. Once stabilized, the DWs should remain due to their topological protection, and could then be manipulated and/or detected by electrical means.

The results presented in "Domain Walls: Electric polarization" allow us to provide a quantitative answer to this question. Since, as shown above, the dipole moment is independent of DW width and rotation profile, an electric field is not expected to affect the shape and size of the DW, assuming that the field is homogeneous over the region where the DW is located. Given the total magnitude of the dipole moment per unit length ($\pi\tilde{f}_{\rm ip}$ or $\pi\tilde{f}_z$ for the in-plane and out-of-plane components, respectively) and DW energy $E_{\rm DW}$, an estimate of the electric field needed to stabilize domains is $\mathcal{E} = \frac{E_{\rm DW}}{\pi\tilde{f}_{\rm ip}} = 0.20$ V/Å $= 2 \cdot 10^4$ kV/cm for an in-plane electric field or $\mathcal{E} = \frac{E_{\rm DW}}{\pi\tilde{f}_z} = 5.0$ V/Å $= 5.0 \cdot 10^5$ kV/cm for an out-of-plane field. While these are large values of

electric fields, taking into consideration magnetostatic dipole-dipole interactions would favor domain formation and lower the electric fields required. Moreover, even an applied field insufficient to make domains energetically favored will increase the probability of their formation during a cooling process. In atomistic spin dynamics simulations, domains formed in CrI_3 monolayers during rapid, zero-field cooling, from above T_C to 0 K in 2 ns[68]. A combination of an applied electric field and rapid cooling should therefore be a viable option to experimentally induce magnetic domains in 2D magnets. If the electric fields can be applied locally, this will also allow control of the position of the DWs. Our calculated electric field-induced DMI parameters provide the necessary prerequisites for further investigations in this direction using atomistic spin dynamics simulations.

In thicker CrI_3 crystals, of a couple of nanometers or thicker, magnetic DWs do form experimentally, and the layers couple ferromagnetically. Our results imply that an electric polarization should appear at these magnetic DWs as well, in principle allowing for their detection and manipulation by electrical means. The precise form of the polarization in thicker samples may, however, differ from that of the monolayers studied here, because of inter-layer coupling and stacking-dependent symmetry breaking.

A few earlier works[21,23,24] have presented computational predictions of the electric polarization of magnetic DWs. The predicted values are mostly of a similar order of magnitude as that found here, ranging from $0.07\mu C/cm^2$ [21] to $0.7\mu C/cm^2$ [23,24]. However, they all rely on a non-relativistic (i.e., neglecting SOC) magnetostrictive phenomena due to the symmetry breaking of a collinear magnetic order. In most magnetic materials, this is not a realistic description of a magnetic DW, where the magnetization gradually rotates over distances much larger than the interatomic spacing. As such, the predictions made here provide a more realistic description of the electric polarization of magnetic DWs than previously available. Unfortunately, little experimental data for magnetic DW polarization is available so far.

Skyrmions: Magnetization texture

Magnetic Skyrmions are another type of magnetic topological soliton where the magnetization texture breaks inversion symmetry. This leads to an electric polarization in insulating materials, as has been experimentally observed in GaV_4S_8[14]. In atomically thin magnets, the out-of-plane polarization may survive even in metallic materials. The electric polarization of Skyrmions in GaV_4S_8 was explained by atomistic magnetoelectric models similar to Eq. (1), but with additional symmetric contributions appearing due to the broken SI symmetry[14,74] (see also Supplementary Note 1). As we will see in the following, the continuum magnetoelectric model is particularly insightful in describing the electric polarization and the net electric dipole moment carried by Skyrmions.

A Skyrmion magnetization texture is conveniently described in polar coordinates $\mathbf{M}(\mathbf{r}) = (\sin\Theta\cos\Phi, \sin\Theta\sin\Phi, \mathcal{P}\cos\Theta)$, at position $\mathbf{r} = (r\cos\phi, r\sin\phi)$, relative to the center of the Skyrmion[11,75]. The polar angle $\Theta(r,\varphi)$ fulfills $\Theta(0,\varphi) = \pi$ and $\Theta(r,\varphi) \to 0$ for large r. The azimuthal angle $\Phi(r,\varphi)$ is periodic $\Phi(r,\varphi) = \Phi(r,\varphi + 2\pi v)$ with integer v. We consider Skyrmions with $\Theta = \Theta(r)$ only dependent on r, and $\Phi(\varphi) = v\varphi + \gamma$, as is appropriate for a continuum description of an isolated Skyrmion in a material that is isotropic in the plane, such as CrI_3. Here, v is vorticity (integer), and γ is helicity, while $\mathcal{P} = \pm 1$ is polarity. Skyrmions are characterized by the integer Skyrmion number

$$Q = \frac{1}{4\pi}\int d^2\mathbf{r}\,\mathbf{M}\cdot\left(\frac{\partial\mathbf{M}}{\partial x}\times\frac{\partial\mathbf{M}}{\partial y}\right) = v\mathcal{P}. \tag{20}$$

We will primarily consider $\mathcal{P} = +1$ and denote $Q = v = +1$ structures as Skyrmions, and those with $Q = v = -1$ as anti-Skyrmions.

In order to illustrate a number of basic properties of the (anti)-Skyrmions, in the next subsections, we shall initially assume a fixed radial form factor of the skyrmion that is independent of its size. This means using the following *Ansatz* for $\Theta(r)$,

$$\Theta(r) = \theta(r/w), \tag{21}$$

where w defines the length scale. This assumption yields a qualitatively correct picture for most properties we are interested in, and allows for an easier understanding of the main mechanisms at work. In practice, we shall use the form[11]

$$\theta(x) = 4\arctan(e^{-x}), \tag{22}$$

which mimics the DW solution derived in the previous section. The rationale behind this choice lies in the fact that the skyrmion, in the limit of a large size, resembles a DW structure with cylindrical symmetry. Note that, unless otherwise specified, our formal results in the remainder of this Section do not assume either Eq. (21) or Eq. (22). In any case, we shall relax this assumption in "Variational Skyrmion solution", where we benchmark our conclusions against the exact solution for an isolated Skyrmion emerging from the continuum equations.

A representative illustration of the magnetization textures associated with an anti-Skyrmion ($v = -1$) and a Skyrmion ($v = +1$) is shown in Fig. 5a and d, respectively, with arrows showing the in-plane component of magnetization and colors showing the out-of-plane component. The case shown is $\gamma = 0$, i.e., a Néel Skyrmion, whereas changing the value to $\gamma = \pi/2$ would rotate the spins to form a Bloch Skyrmion.

Skyrmions: Polarization texture

Application of Eq. (4) to the Skyrmion magnetization, in the appropriate polar coordinates, leads to an electric polarization

$$\begin{aligned}\mathbf{P} \;=\; & \mathcal{P}\Big(-\tilde{f}_{\rm ip}\cos\big[(v+1)\varphi+\gamma\big]F_v^-(r)\,,\,\tilde{f}_{\rm ip}\sin\big[(v+1)\varphi+\gamma\big]F_v^-(r),\\ & \tilde{f}_z\cos\big[(v-1)\varphi+\gamma\big]F_v^+(r)\Big) \;+\tilde{f}_{12,12}\tfrac{v}{r}\sin^2\Theta\big(\cos\varphi,\sin\varphi,0\big),\\ & \text{where}\;\; F_v^{\pm}(r) = \tfrac{1}{2r}\big\{v\sin(2\Theta)\pm 2r\Theta'(r)\big\},\end{aligned} \tag{23}$$

from which several interesting observations can be made. First, we can characterize the topological properties of the in-plane components of $\mathbf{P}$ via the concept of vorticity[76]

$$N_P = \frac{1}{2\pi}\oint_C d\mathbf{l}\cdot\frac{d\Phi_P}{d\mathbf{l}} = -(v+1) \tag{24}$$

where Φ_P is the angle between the polarization and $\hat{x}$, and the closed path C is arbitrary provided that it contains the center of the Skyrmion. (This is in all respects equivalent to Eq. (18), only applied to a closed path in open boundary conditions.) Thus, the (in-plane projection of the) polarization, which has contributions from two terms, respectively due to $\tilde{f}_{\rm ip}$ and $\tilde{f}_{12,12}$, inherits a v-dependent vorticity from the topology of the magnetization texture. The first term alone would give precisely $N_P = -(v+1)$, whereas the second term alone would give a v-independent winding of $N_P = 1$, which, however, vanishes when both terms are considered together. That is, taking the integral in Eq. (24), including both terms, along, for example, a circular path at small r, one finds the result $N_P = -(v+1)$ determined entirely by the winding of the dominating first term.

The right part of Fig. 5 shows the polarizations from Eq. (23) (middle-right), for an anti-Skyrmion with $v = -1$ (top) and a Skyrmion with $v = 1$ (bottom). Fig. 5b and e illustrate the $N_P = 0$ and $N_P = -2$ polarization vorticity of the Skyrmion and anti-Skyrmion, respectively. Integration of the in-plane polarization yields a non-zero net dipole moment only when $N_P = 0$, i.e., for the anti-Skyrmion with $v = -1$, while it is zero for the Skyrmion. Thus, we expect that the net electric dipole moment (areal integral of the polarization) should point in-plane for the anti-Skyrmion. The out-of-plane polarization component P_z, shown in Fig. 5c and f, instead has an angular

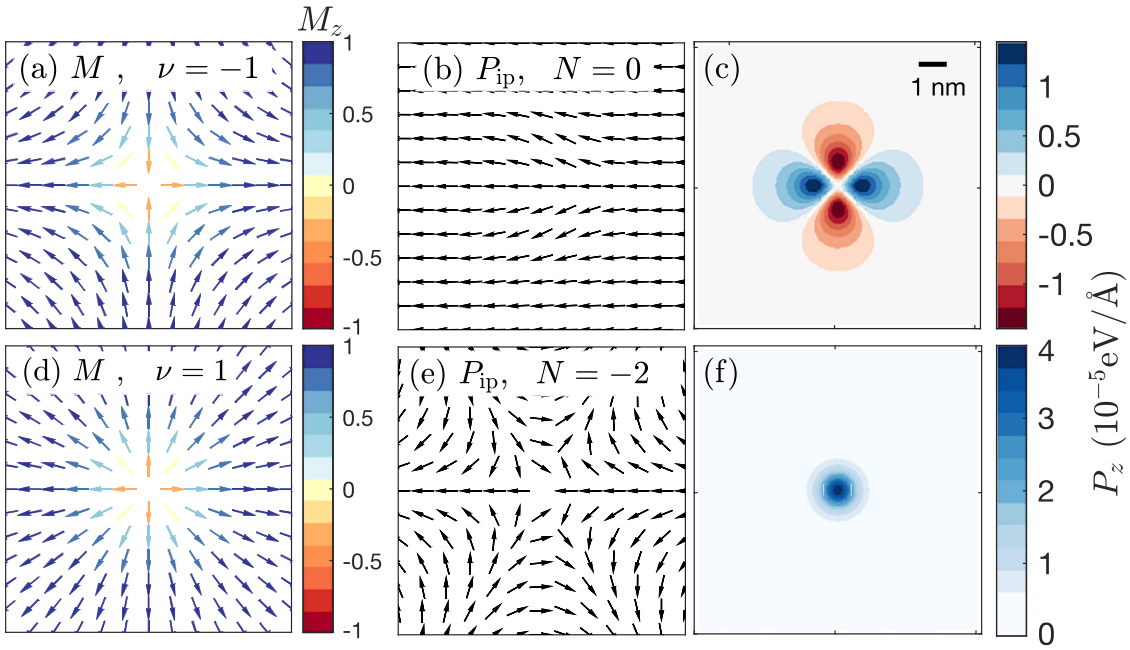

Fig. 5 | The Magnetization texture and electric polarization of (anti-)Skyrmions. The top row **a**–**c** shows an anti-Skyrmion ($\nu = -1$) and the bottom row **d**–**f** a Skyrmion ($\nu = 1$), both with $\gamma = 0$. The first column (**a**, **d**) shows the magnetization with the in-plane direction as arrows and the out-of-plane component represented by color. The middle column (**b**, **e**) shows the in-plane direction of the electric polarization, and the third column (**c**, **f**) shows the out-of-plane component of polarization, P_z.

dependence of the form $(\nu-1)\varphi$, as seen in Eq. (23). Hence, P_z of the anti-Skyrmion, shown in Fig. 5c, has equal positive and negative regions, and its integral, i.e. the net dipole moment in the z-direction, is zero. The Skyrmion case in Fig. 5f, on the other hand, has full 2D rotational symmetry and a non-zero out-of-plane dipole moment.

Skyrmions: Dipole moment

We confirm the above observation by calculating the net electric dipole moment of a general Skyrmionic magnetization texture

$$\mathbf{p} = \int \mathbf{P}(\mathbf{r})\mathrm{d}^2\mathbf{r} = \begin{cases} p_{\rm ip}(-\cos\gamma, \sin\gamma, 0)\mathcal{P}, & \text{if } \nu = -1 \\ p_z(0,0,\cos\gamma)\mathcal{P}, & \text{if } \nu = +1 \\ 0, & \text{if } \nu \neq \pm 1 \end{cases} \quad (25)$$

where $p_{\rm ip} = 2\pi\tilde{f}_{\rm ip}\int rF^{-}_{-1}(r)\mathrm{d}r$ and $p_z = 2\pi\tilde{f}_z\int rF^{+}_{1}(r)\mathrm{d}r$ are the magnitudes of the in-plane and out-of-plane Skyrmion dipole moments (the z-component is also scaled by $\cos\gamma$). Thus, a non-zero net electric dipole moment only appears for Skyrmions and anti-Skyrmions with $\nu = \pm 1$, while it is zero for all higher-order (anti-)Skyrmions ($|\nu| > 1$). The anti-Skyrmion ($\nu = -1$) has an in-plane dipole moment with direction determined by γ, while the Skyrmion $\nu = 1$ has an out-of-plane dipole moment with magnitude and direction determined by γ. In both cases, the polarity $\mathcal{P}$, flips the sign of the electric dipole moment. These results hold qualitatively for any material with the same crystal symmetry as CrI_3 and any Skyrmion radial profile $\Theta(r)$, while it can differ for other crystal symmetries, where the results should be re-derived using the correct form of the tensor $\tilde{f}_{ij,\alpha\beta}$. The high-symmetry (e.g., cubic) case is obtained by setting $\tilde{f}_{12,12} = \tilde{f}_z$ and $\tilde{f}_{\rm ip} = 0$. Then, only the net out-of-plane electric dipole moment for Skyrmions ($\nu = +1$) remains non-zero, which is a universal feature of all (insulating or 2D) materials hosting Skyrmions. The in-plane dipole moment of anti-Skyrmions, on the other hand, vanishes in the cubic case and is non-zero in specific crystallographic point groups where $\tilde{f}_{\rm ip}$ is symmetry allowed (See Supplementary Note 2).

In the specifics of our fixed-shape skyrmion model, the dipole moment is a linear function $p_i = d_i w$ of the size w, where d_i is proportional to $\tilde{f}_i$, and i is either z or in-plane. To see this, we can define a Skyrmion radius w in line with Eq. (21) and write the radial profile in terms of a dimensionless radial coordinate $\rho = r/w$, $\Theta(\rho) = \Theta(r/w)$; then, derivatives yield factors $1/w$ while surface integration gives w^2 (See Eq. (35) for an expression for d_i in terms of $\Theta(r)$ and the materials parameters). Using the ansatz in Eqs (22), we find numerical values $d_{\rm ip} = 37 \cdot 10^{-3}e$ and $d_z = 1.5 \cdot 10^{-3}e$ for the in-plane dipole moment of the anti-Skyrmion or out-of-plane dipole moment of the Skyrmion, respectively. The results imply that large (anti-)Skyrmions carry a large electric dipole moment. We shall see in the following Section that this leads to a large amount of energy by coupling to an applied electric field.

Skyrmions: Energetics

In the absence of DMI/electric fields, the magnetic energy (Eq. (8)) of an (anti-)Skyrmion in a material with uniaxial magnetic anisotropy, such as CrI_3 is, within the length-scale *Ansatz* of Eq. (21),

$$E = E_{\rm Sk} - E_{\rm FM} = a + kw^2, \quad a,\ k > 0. \quad (26)$$

This follows from the same arguments as those above, which led to the dipole moment being proportional to w. Within the specific choice of form factor given by Eq. (22), we find numerical values of $a = 0.4$ meV and $k = 0.4$ meV/Å^2 (see Methods, "Skyrmion Solution with Electric Field/DMI"). Eq. (26) implies that if a (anti-)Skyrmion were to form, it would shrink to zero radius (i.e., the lowest-energy state respecting the topology). A numerical illustration of this outcome is provided in Fig. 6, where Eq. (26) is plotted as a red line, with the values for a and k given above. The zero radius "needle"-like (anti-)Skyrmion would have energy a, related to the spin stiffness. Next, we will see how the magnetoelectric coupling of an applied electric field to the dipole moment described in the previous section affects this situation.

As seen above, the (anti-)Skyrmions will carry an electric dipole moment $p = dw$, whereby a uniform applied electric field lowers the energy of the (anti-)Skyrmion by the dipole energy

$$E_{\rm dip} = -\mathcal{E}\int \mathbf{P}(\mathbf{r})\mathrm{d}^2\mathbf{r} = -\mathcal{E}dw, \quad (27)$$

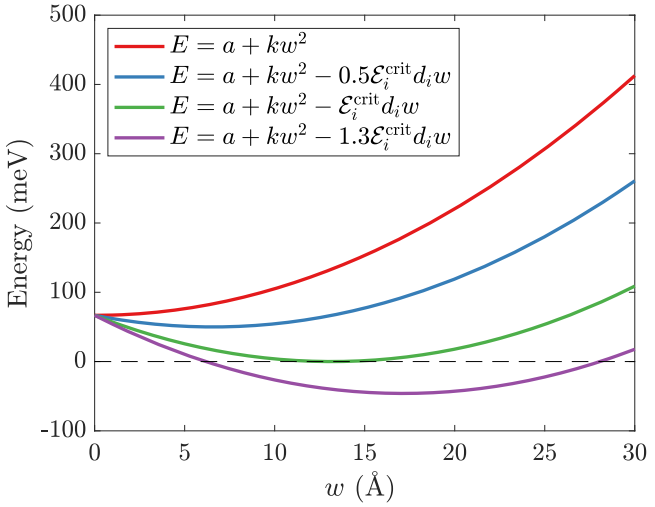

Fig. 6 | Skyrmion energy as a function of size w at different applied electric fields. The (anti-)Skyrmion energy relative to the ferromagnetic state, evaluated with $\Theta(r) = 4\arctan(e^{-r/w})$, is plotted as a function of w, considering exchange and anisotropy energy, and coupling to an applied electric field, expressed in terms of the critical field $\mathcal{E}_i^{\rm crit} = 2\sqrt{ak}/d_i$.

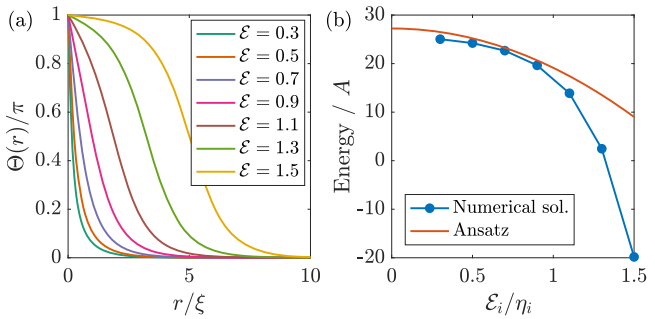

Fig. 7 | Skyrmion solutions for different applied electric fields. a The radial profile $\Theta(r)$ that solves Eq. (36) for (anti-)Skyrmions at a certain electric field $\mathcal{E}$ in units of η_i, corresponding to an induced DMI $\mathcal{D}_i = |\tilde{f}_i|\mathcal{E}_i$ (i denoting z or in-plane, depending the field direction). **b** Energy, relative to the FM state, of the solutions presented in (**a**) for (anti-)Skyrmions as a function of applied field (blue line, circles). The result $E = a - \frac{(d\mathcal{E})^2}{4k}$ from the Ansatz $\Theta(r) = \arctan(e^{-r/w})$ is shown for comparison (orange line).

where the last equality holds assuming the Skyrmion has one well-defined length scale of w (Eq. (21)). As we have seen, an equivalent way to view this energy gain is that an electric field induces DMI, which favors (anti-)Skyrmion formation. There will, however, be a competition between this energy gain and the other terms in the magnetic energy [magnetic exchange and anisotropy of Eq. (26), shown with a red line in Fig. 6], all of which should be considered together to assess the possibility of electric field stabilization of Skyrmions. Combining Eq. (27) with the energy in Eq. (26), leads to a simple second-order polynomial $E(w) = a - \mathcal{E}_i d_i w + kw^2$ for the energy as a function of Skyrmion size w under applied electric field $\mathcal{E}_i$, in direction i. This is also plotted for a few electric field values in Fig. 6, from which we can now present simple schematic arguments regarding the stability of (anti-) Skyrmions in electric fields; at zero field, the lowest energy Skyrmion state is that with zero radius. An applied electric field shifts the energy minimum to larger values of $w = \frac{d}{2k}\mathcal{E}$, leading to metastable Skyrmion states with radius proportional to the magnitude of the field. At sufficiently large electric fields, the energy minimum becomes negative, and (anti-)Skyrmions are lower in energy than the FM state. The critical field in this model is $\mathcal{E}_i^{\rm crit} = 2\sqrt{ak}/d_i$, where the energy minimum is exactly at zero, so a single Skyrmion state is degenerate with the FM state. Numerically, with the materials parameters found for CrI_3, we find $\mathcal{E}_{\rm ip}^{\rm crit} = \frac{2\sqrt{ak}}{d_{\rm ip}} = 0.27$ V/Å for an in-plane field stabilizing an anti-Skyrmion, and $\mathcal{E}_z^{\rm crit} = \frac{2\sqrt{ak}}{d_z} = 6.7$ V/Å for an out-of-plane field stabilizing a Skyrmion. Note that in both cases the Skyrmion size at the critical field is $w = \sqrt{a/k} \approx 1.646\sqrt{A/K} = 13$ Å. While these are very large electric fields, at least the one for the in-plane case may be realistically achievable in experiments. Smaller electric fields would already be sufficient to stabilize finite-size Skyrmions as metastable states. Moreover, these critical fields are expected to be overestimated because of magnetostatic dipole interactions, which would lower the energy of these spin textures relative to the ferromagnetic state. Additionally, the calculations relied on the radial profile $\Theta(r) = 4\arctan(e^{-r/w})$ which does not describe the true stationary state of the (anti-)Skyrmion solutions, therefore overestimating their energies. In the following Section, we improve our description by numerically minimizing the magnetic energy functional under an applied electric field, providing a correct radial profile.

Variational Skyrmion solution

The energy density contribution from the coupling of a (uniform) electric field to the magnetic texture is given by the middle expression in Eq. (27) (equivalent to an electric field induced DMI term) added to Eq. (8). By numerically minimizing the energy functional (see Eq. (34)) we find solutions for $\Theta(r)$, plotted in Fig. 7a, and corresponding energies in Fig. 7b. Note that the solutions only depend on the magnitude of the electric field-induced DMI value $|\mathcal{D}_i| = |\tilde{f}_i\mathcal{E}_i|$. Thus, an in-plane electric field $\mathcal{E}_{\rm ip}$ gives an anti-Skyrmion with an identical radial profile and energy as that of a Skyrmion in an out-of-plane field $|\mathcal{E}_z| = |\mathcal{E}_{\rm ip}\frac{\tilde{f}_{\rm ip}}{\tilde{f}_z}|$. With the field expressed in terms of the electric field unit $\eta_i = \frac{A}{|\tilde{f}_i|\xi}$, the energy plotted in Fig. 7b is thus identical for the two cases, but the unit is different for the different field directions, η_z = 3.9 V/Å and $\eta_{\rm ip}$ = 0.16 V/Å. The results qualitatively confirm the arguments above; the Skyrmion radius increases with the magnitude of the applied electric field, and the energy of the (anti-)Skyrmion solution decreases with increasing field, eventually allowing solutions that are lower in energy than the FM state. Since the electric field here is a parameter that linearly scales the magnitude of the DMI, the results can more generally be understood as a larger DMI favors (anti)-Skyrmion formation but also increases the equilibrium size of the (anti)-Skyrmion. As it should, the energy of the correct numerical solution is lower than that obtained with the ansatz (Eq. (22)), which is also plotted for comparison in Fig. 7b. Hence, the critical field of the transition is also reduced in comparison to the previous estimate, to a value of $\mathcal{E}_i = 1.32\eta_i$, or approximately 5.2 V/Å and 0.2 V/Å for the Skyrmion or anti-Skyrmion stabilized by out-of-plane and in-plane fields, respectively.

Previous work, using DFT calculations under a finite electric field in combination with atomistic spin dynamics simulations, argued that an out-of-plane electric field of 0.2 V/Å is sufficient to stabilize Skyrmions in CrI_3[17]. This was questioned in the subsequent work of Ghosh et al., finding that a 45 times larger field would be needed[25]. Our results are consistent with those of Ghosh et al. in the case of an out-of-plane electric field. Interestingly, our results indicate the previously overlooked possibility, *i.e.*, to stabilize anti-Skyrmions using an in-plane electric field, is possible at significantly lower field strengths.

Energetics of the different phases

For each of the non-collinear spin textures discussed above (spirals, DWs, Skyrmions) there is a critical DMI, and corresponding critical electric field, at which these structures become lower in energy relative to the FM state, as summarized in Table 1. Interestingly, the critical field is very similar for the three types of spin states. The comparison in energy between the three types of spin states above the critical field is not straightforward as it depends on the density of DWs and Skyrmions. Spin spirals and DWs have equivalent magnetization windings and are indistinguishable at high DW densities, which would be favored at large homogeneous fields. Thus, a homogeneous

Table 1 | Critical electric field in the in-plane or out-of-plane (*z*) direction, to stabilize spin spirals, DWs, or Skyrmions, relative to the FM state

	Spiral	DW	Skyrmion Ansatz	Skyrmion
$\mathcal{E}_{ip}$ (V/Å)	0.22	0.20	0.27	0.21
$\mathcal{E}_z$ (V/Å)	5.5	5.0	6.7	5.2
$\mathcal{D}$ (eV/Å)	0.43	0.42	0.55	0.41

The Skyrmion values are given based on the ansatz $\Theta(r) = 4\arctan(e^{-r/w})$, and the numerical solution for $\Theta(r)$ (rightmost column). The corresponding critical DMI $\mathcal{D} = \tilde{f}_{ip}\mathcal{E}_{ip} = \tilde{f}_z\mathcal{E}_z$ is also listed.

electric field would likely favor a spin spiral state, rather than DWs. However, one can envisage that an electric field applied locally along a line could stimulate the appearance of an isolated DW. For the (anti-)Skyrmions, it is again difficult to give precise statements of their stability relative to spin spirals. However, Skyrmion states are routinely stabilized over spiral states using applied magnetic fields[12]. Thus, a combination of applied electric and magnetic fields is a viable path to (anti-)Skyrmion stabilization. Alternatively, one could again consider a locally applied electric field, e.g., over a circular region, as a possible path to stabilize (anti-)Skyrmions. Further investigations in these directions are of interest for future follow-up studies. Note that, as was shown in Fig. 2, even a small in-plane electric field will induce a small antiferromagnetic order parameter, proportional to the field strength.

Discussion

We have presented a multiscale approach to magnetoelectricity, connecting atomistic and continuum descriptions, suitable at different length scales. We determined all parameters of the models from first principles DFT calculations and validated that they accurately describe the electric polarization of complex spin textures, such as spin spirals. We also showed that the parameters of the model are equivalent to the electric field-induced DMI, known to stabilize a variety of non-collinear magnetic phases, including topologically protected solitons, such as Skyrmions. Using this approach, we have studied the coupling of electric fields to topological solitons in the 2D ferromagnet CrI_3. In particular, we investigated the possibility to stabilize domain walls or (anti-)Skyrmions. Earlier studies regarding the effect of electric fields on 2D magnets often focused on out-of-plane fields[77,78]. Interestingly, here we find that in-plane electric fields couple more strongly (by more than an order of magnitude) to the magnetism of CrI_3 than out-of-plane fields. Moreover, we showed that the net electric dipole moment of Skyrmions is out-of-plane while that of anti-Skyrmions is in-plane, whereby stabilization of anti-Skyrmions using an in-plane electric field may be a viable possibility in CrI_3.

While the electric field needed to stabilize topological magnetic solitons found here is large, their formation could be stimulated by cooling samples under an applied field, after which they would be topologically protected and expected to remain in the sample. Locally applied fields, then, would enable the stabilization and control of Skyrmions and DWs. Moreover, in the calculations presented here, magnetostatic dipole-dipole interactions were neglected. Although these are expected to be of less importance in 2D magnets, compared to the 3D case, they could contribute to stabilizing the non-collinear spin textures considered here over the FM state. In particular, they have been found to favor Skyrmion formation in ultrathin magnetic films by effectively reducing the perpendicular magnetic anisotropy[77,78]. The effect of temperature and applied magnetic fields would also be interesting to study. Given that the electric field-induced DMIs are available from the magnetoelectric models considered here, these topics would be feasible for future studies, e.g., using atomic spin dynamics simulations[60]. In addition to their importance for electric field engineering of topological magnetic solitons in 2D magnets, the results, together with recent studies effects of curvature on magnetism[37], provide a promising starting point for exploring the intriguing relationship between magnetoelectric effects and flexomagnetism, potentially opening up an exciting new, rich research landscape with a flexomagnetoelectric interplay between magnetism, electric polarization, and curvature.

Methods

Macroscopic polarization induced by spiral magnetism within the atomistic approach

The starting point for developing an atomistic theory of spin-induced polarization is assuming that the macroscopic polarization can be decomposed as a sum of atomic (local) and pairwise contributions involving two spins, and then considering the polarization of a general non-collinear configuration of each spin dimer[44,46,47]. The dipole induced by each spin dimer can then be expanded as a Taylor series of spin components, where only the lowest orders are retained[46,47]. In the most general case, the macroscopic polarization can then be written as:

$$\boldsymbol{P} = \frac{1}{V}\left\{\sum_i \boldsymbol{S}_i \cdot \mathcal{P}^i \cdot \boldsymbol{S}_i + \frac{1}{2}\sum_{ij} \boldsymbol{S}_i \cdot \mathcal{P}^{ij} \cdot \boldsymbol{S}_j\right\}, \tag{28}$$

where V is the (macroscopic) volume, i runs over all lattice sites and j over all neighbors for each given site, that is typically restricted to a few nearest-neighbor shells, while the prefactor 1/2 is introduced to count each bond contribution only once. $\mathcal{P}^i$ and $\mathcal{P}^{ij}$ relate the localized spins to polarization, being both rank-three polar tensors with elements of the form $\mathcal{P}_{\alpha\beta\gamma}$, where α is the polarization component induced by the coupling of spin components β and γ. The intrasite coupling tensor is symmetric under the exchange of the second and third Cartesian indices, while the intersite coupling tensor can be decomposed into a symmetric and antisymmetric part with respect to the β, γ indices:

$$\begin{aligned}\mathcal{P}^{ij}_{\alpha\beta\gamma} &= \tfrac{1}{2}\left[\mathcal{P}^{ij}_{\alpha\beta\gamma} + \mathcal{P}^{ij}_{\alpha\gamma\beta}\right] + \tfrac{1}{2}\left[\mathcal{P}^{ij}_{\alpha\beta\gamma} - \mathcal{P}^{ij}_{\alpha\gamma\beta}\right] \\ &\equiv (\mathcal{P}^{ij}_{\alpha\beta\gamma})^S + (\mathcal{P}^{ij}_{\alpha\beta\gamma})^A.\end{aligned} \tag{29}$$

The antisymmetric part can be expressed in a more compact form as $\boldsymbol{S}_i \cdot (\mathcal{P}^{ij})^A \cdot \boldsymbol{S}_j = \mathcal{M}^{ij}(\boldsymbol{S}_i \times \boldsymbol{S}_j)$, where the $\mathcal{M}^{ij}$ is now a rank-two polar tensor (3 × 3 matrix) with elements $\mathcal{M}_{\alpha\beta} = \epsilon_{\beta\gamma\delta}\mathcal{P}_{\alpha\gamma\delta}$, with $\epsilon_{\beta\gamma\delta}$ the Levi-Civita symbol and assuming summation over repeated indices. The latter then takes the form of a generalized KNB coupling, describing the electric polarization induced by the spin-current mechanism[47]. Microscopically, the intrasite contribution has been related to the spin-dependent p-d hybridization mechanism, responsible, e.g., for magnetically induced ferroelectricity in the collinear antiferromagnet $Ba_2CoGe_2O_7$[79,80]. The symmetric intersite contribution, instead, has been shown to account for the electronic contribution to type-II multiferroicity in collinear magnets such as $HoMnO_3$[54,65], microscopically arising from a subtle interplay between magnetic and orbital ordering[81]. It also contributes to the electric polarization of Skyrmions in multiferroic GaV_4S_8[74], where it is symmetry allowed due to the inversion asymmetric crystal structure.

We now analyse the general form of the macroscopic polarization induced by a helimagnetic configuration. For a crystalline periodic lattice, the atomic positions are given by $\boldsymbol{r}_i \equiv \boldsymbol{r}_{nl} = \boldsymbol{R}_n + \boldsymbol{\tau}_l$, where $\boldsymbol{R}_n$ is the lattice vector of the n^{th} cell and $\boldsymbol{\tau}_l$ denotes the atomic position within the unit cell, while $V = N\Omega$, N being the total number of cells, each with a volume Ω (area in 2D crystals). A general non-collinear spin modulation with wave vector $\boldsymbol{q}$ can be expressed as:

$$\boldsymbol{S}(\boldsymbol{r}_{nl}) = s_1\boldsymbol{e}_1\cos(\boldsymbol{q}\cdot\boldsymbol{r}_{nl}) + s_2\boldsymbol{e}_2\sin(\boldsymbol{q}\cdot\boldsymbol{r}_{nl}) + s_3\boldsymbol{e}_3, \tag{30}$$

where $\boldsymbol{e}_i$ are unit vectors forming an orthogonal basis. Eq. (30) describes a sinusoidal spin-density wave if only s_1 or s_2 is nonzero, an (elliptical) helix if only s_3 is zero, and a conical (elliptical) helix when all s_i coefficients are nonzero. Plugging Eq. (30) in Eq. (28) and taking the thermodynamic limit

$N \to \infty$, one gets:

$$\boldsymbol{P} = \frac{1}{\Omega}\sum_l \Big\{ \frac{1}{2}\left[s_1^2\, \boldsymbol{e}_1 \cdot \mathcal{P}^l \cdot \boldsymbol{e}_1 + s_2^2\, \boldsymbol{e}_2 \cdot \mathcal{P}^l \cdot \boldsymbol{e}_2 + 2 s_3^2\, \boldsymbol{e}_3 \cdot \mathcal{P}^l \cdot \boldsymbol{e}_3 \right] + \frac{1}{2}\sum_j s_3^2\, \boldsymbol{e}_3 \cdot \left(\mathcal{P}^{lj}\right)^S \cdot \boldsymbol{e}_3 + \frac{1}{4}\sum_j \Big[s_1^2\, \boldsymbol{e}_1 \cdot \left(\mathcal{P}^{lj}\right)^S \cdot \boldsymbol{e}_1 + s_2^2\, \boldsymbol{e}_2 \cdot \left(\mathcal{P}^{lj}\right)^S \cdot \boldsymbol{e}_2 \Big] \cos(\boldsymbol{q}\cdot\boldsymbol{r}_j) + \frac{1}{2}\sum_j s_1 s_2\, \mathcal{M}^{lj}(\boldsymbol{e}_1 \times \boldsymbol{e}_2)\, \sin(\boldsymbol{q}\cdot\boldsymbol{r}_j) \Big\}. \tag{31}$$

Both the intrasite and symmetric intersite contributions clearly describe the polarization induced by the collinear components of the spin configuration, whereas the contribution due to noncollinear components is fully accounted for by the antisymmetric intersite coupling tensor, describing a generalized spin-current (gKNB) mechanism, in agreement with earlier conclusions drawn for an isolated spin dimer[46]. Additionally, crystal symmetries can introduce further constraints on the allowed contributions to macroscopic polarization. The symmetry requirements on the individual intra- and intersite terms will depend on the site and bond symmetry, respectively, and they are addressed in Supplementary Note 1. Crystal symmetries also determine the transformation rules for the coupling tensors of symmetry-equivalent sites and bonds. When inversion symmetry is a space-group element of the crystal, each site/bond will have an inversion-partner, each carrying an equal and opposite intrasite/intersite contribution, given the polar character of both $\mathcal{P}^l$ and $\mathcal{P}^{lj}$. The corresponding intrasite contributions will clearly cancel out exactly. The symmetric intersite contribution will also cancel out, given the cosinusoidal (even) dependence on the helical spin modulation, leaving only the antisymmetric term depending instead on $\sin(\boldsymbol{q}\cdot\boldsymbol{r}_j)$. Therefore, the macroscopic polarization induced by a noncollinear helimagnetic configuration in centrosymmetric crystals can be univoquely expressed as in Eq. 1 of the main text.

Given Eq. (28), we can generalize Eq. (3) as

$$\mathcal{P}^{ij}_{\alpha\beta\gamma} = \frac{\partial \mathcal{J}^{ij}_{\beta\gamma}}{\partial \mathcal{E}_\alpha}, \tag{32}$$

where $\mathcal{J}^{ij}_{\alpha\beta}$ is the tensorial form of the exchange interaction, describing the energy of two interacting spins $\mathbf{S}^i$ and $\mathbf{S}^j$ as $E_{ij} = \mathcal{J}^{ij}_{\alpha\beta} S^i_\alpha S^j_\beta$[82]. The DMI is the anti-symmetric part of $\mathcal{J}^{ij}_{\alpha\beta}$. That only the anti-symmetric part of $\mathcal{P}^{ij}_{\alpha\beta\gamma}$ gives a macroscopic polarization in centrosymmetric crystals, then corresponds to only the DMI coupling linearly to a uniform electric field. Correspondingly, in non-centrosymmetric crystals, one may expect a linear coupling also between other components of $\mathcal{J}^{ij}_{\alpha\beta}$ to uniform electric fields.

First-principles calculations and computational parameters

In order to determine all parameters of the atomistic model in Eq. (1), which are then used to determine the continuum parameters, we use density functional theory (DFT) calculations. Calculations are performed using the projector augmented wave (PAW)[83,84] method, as implemented in VASP[85–87], with settings in accordance with earlier work[37,88]. The local density approximation (LDA) is used for the exchange-correlation together with an additional Coulomb repulsion[89] of $U = 0.5$ eV on Cr d-states. It has previously been shown that different choices of the exchange-correlation functional qualitatively give the same results for the magnetic properties of CrI_3, with moderate quantitative changes[90,91]. Still, we recalculated selected results in the generalized gradient approximation[92] and confirmed that this is the case also for the magnetoelectric properties considered here. Calculations for an isolated monolayer are performed within periodic boundary conditions, with (at least) 15 Å of vacuum separating the repeated monolayer images. Constrained, non-collinear magnetic calculations, with SOC, were done using a penalty energy for spins deviating from the desired configuration[93,94]. We checked that the results are insensitive to the value of the penalty energy. The calculations of the magnetoelectric tensor of Eq. (1) were done in a $3 \times 3 \times 1$ supercell with a $6 \times 6 \times 1k$-point grid. We also present validations of the models using direct DFT calculations for the polarization of spin spirals. These refer to spin spirals with wavevector $q = \frac{2\pi}{L}$, performed in a supercell of dimension $a \times L$ or $\sqrt{3}a \times L$, for propagation in the x or y-direction, respectively, where $a = 6.71$ Å is the lattice constant. The electric polarization is evaluated with the Berry phase formalism[95] in all cases.

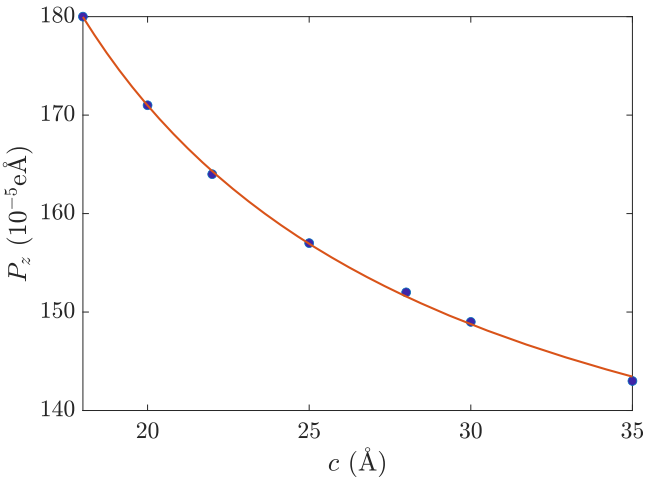

Fig. 8 | Scaling of the out-of-plane electric polarization with vacuum distance. P_z calculated as a function of the distance c between adjacent monolayer periodic images, for one spin configuration, including a fitting of the form $P_z(c) = \frac{P_z(c\to\infty)}{1-\frac{\alpha_\perp}{\epsilon_0 c}}$, leading to $\alpha_\perp = 5.5 \cdot 10^{-21}$ F.

Electrical boundary conditions

Since the couplings discussed here involve the macroscopic electrical polarization, the electrical boundary conditions (EBC) need to be specified in their definition. For a 3D crystal, the most natural choice is to assume short-circuit EBC, consistent with the extended nature of the system in all directions. This choice is automatically enforced by the assumption of periodicity in standard first-principles codes, and does not require any special treatment.

In the case of an isolated 2D layer, which will be our main focus in the remainder of this work, the most natural choice for the EBC consists of assuming free boundary conditions[96]. This requires some care, as it requires in principle a truncated Coulomb kernel[96–99], which at the zone center (relevant to the macroscopic polarization targeted in this work) boils down to applying a dipole correction in the vacuum layer. In this work, we find it more practical to perform all our calculations within the standard 3D electrostatic kernel and correct a posteriori for the spurious unphysical interaction between images. More specifically, we extrapolate the z-component of the polarization to the limit of infinite vacuum using the expression

$$P_z(c) = \frac{P_z(c \to \infty)}{1 - \frac{\alpha_\perp}{\epsilon_0 c}}, \tag{33}$$

where c is the distance between neighboring monolayers and $\alpha_\perp$ is the out-of-plane polarizability of the layer at frozen spins[96]. By varying the interlayer distance c in the range 17.5 Å to 35 Å, we find an essentially perfect fit to Eq. (33) with $\alpha_\perp = 5.5 \cdot 10^{-21}$F, as shown in Fig. 8.

Skyrmion solution with electric field/DMI

The total magnetic energy functional, including electric field-induced DMI, is obtained by adding $\mathcal{D} = -\mathcal{E} \cdot \mathbf{P}(\mathbf{r})$ to the energy density in Eq. 8 of the

main text (for $v = \pm 1$)

$$E = 2\pi A \int_0^\infty r\left([\Theta'(r)]^2 + \left(\frac{1}{r^2}+\frac{1}{\xi^2}\right)\cdot\sin^2\Theta - \left|\frac{\mathcal{E}_i}{\eta_i}\right|\frac{1}{\xi}\left[\Theta'(r)+\frac{\sin 2\Theta}{2r}\right]\right)\mathrm{d}r \tag{34}$$

$$= \underbrace{2\pi A\int_0^\infty \rho\left([\Theta'(\rho)]^2+\frac{1}{\rho^2}\sin^2\Theta\right)\mathrm{d}\rho}_{a} + \underbrace{2\pi K\int_0^\infty \rho\sin^2\Theta\mathrm{d}\rho}_{k} w^2 - |\mathcal{E}_i|\underbrace{2\pi|\tilde{f}_i|\int_0^\infty \rho\left(\Theta'(\rho)+\frac{\sin 2\Theta}{2\rho}\right)\mathrm{d}\rho}_{d_i} w \tag{35}$$

where $\tilde{f}_i$ is either $\tilde{f}_{\mathrm{ip}}$ or $\tilde{f}_z$, depending on whether the electric field is oriented in or out of plane. Here, we introduce the direction-dependent electric field unit $\eta_i = \frac{A}{|f_i|\xi} = \frac{\sqrt{AK}}{|f_i|}$. In Eq. (35), we made the variable substitution $\rho = r/w$ to illustrate the meaning of a, d, and k. The helicity γ and polarity $\mathcal{P} = \pm 1$ are assumed to adapt themselves to maximize the gain in electric dipole energy, i.e., $(-\cos\gamma, \sin\gamma, 0)$ will be (anti-)parallel to the field if it is in-plane, or γ will be either 0 or π if it is out-of-plane. There is no unique combination of values that gives the ground state solution, since changing simultaneously both $\mathcal{P}$ and γ gives different degenerate states. The Euler-Lagrange equation that minimizes Eq. (34) is

$$\xi^2\Theta''(r) + \frac{\xi^2}{r}\Theta'(r) - \frac{1}{2}\sin 2\Theta\left(1+\frac{\xi^2}{r^2}\right) + \frac{\mathcal{E}_i}{\eta_i}\frac{\xi}{r}\sin^2\Theta = 0. \tag{36}$$

Since this equation depends only on ξ and the value of the electric field relative to η_i, Skyrmion solutions for out-of-plane electric fields and anti-Skyrmion solutions for in-plane fields will have identical energy and radial profile $\Theta(r)$ at the same DMI values of $D_i = |f_i|\mathcal{E}_i$. By numerically solving Eq. (36), with a standard finite difference approach, we find the radial profile $\Theta(r)$ and the corresponding energies as functions of electric field, as plotted in Fig. 7 of the main text. Note that we only consider cases with either in-plane or out-of-plane fields, not intermediate directions.

Given the ansatz $\Theta(r) = 4\arctan(\mathrm{e}^{-r})$, we can evaluate the integrals in Eq. (35) to

$$a = 2\pi A(4\ln 2 + I) \tag{37}$$

$$k = \frac{4\pi}{3}K(1+\ln 4) \tag{38}$$

$$d_i = 2\pi f_i\left(\frac{2}{3} - 4C\right), \tag{39}$$

where

$$I = \int_0^\infty \frac{\sin^2\Theta}{r}\mathrm{d}r \approx 1.53971 \tag{40}$$

$$C = \sum_{k=0}^{\infty}\frac{(-1)^k}{(2k+1)^2} \approx 0.91597. \tag{41}$$

Data availability

Any data will be provided upon reasonable request to the authors.

Received: 5 May 2025; Accepted: 4 September 2025;
Published online: 29 September 2025

References

1. Dzyaloshinskii, I. On the magneto-electrical effect in antiferromagnets. *J. Exp. Theor. Phys.* **37**, 881 (1960).
2. Astrov, D. N. The magnetoelectric effect in antiferromagnetics. *J. Exp. Theor. Phys.* **11**, 708 (1960).
3. Baryakhtar, V. G., Lvov, V. A. & Yablonskii, D. A. Inhomogenousmagnetoelectric effect. *JETP Lett.* **37**, 675 (1983).
4. Spaldin, N. A. & Fiebig, M. The renaissance of magnetoelectric multiferroics. *Science* **309**, 391–392 (2005).
5. Spaldin, N. A. & Ramesh, R. Advances in magnetoelectric multiferroics. *Nat. Mater.* **18**, 203–212 (2019).
6. Khomskii, D. Classifying multiferroics: Mechanisms and effects. *Physics* **2** https://physics.aps.org/articles/v2/20 (2009).
7. Tokura, Y. & Seki, S. Multiferroics with spiral spin orders. *Adv. Mater.* **22**, 1554–1565 (2010).
8. Sergienko, I. A. & Dagotto, E. Role of the Dzyaloshinskii-Moriya interaction in multiferroic perovskites. *Phys. Rev. B* **73**, 094434 (2006).
9. Hubert, A. & Schäfer, R. *Magnetic Domains* (Springer-Verlag, Berlin, 1998).
10. Parkin, S.S.P., Hayashi, M. & Thomas, L. Magnetic domain-wall racetrack memory. *Science* **320**, 190–194 (2008).
11. Bogdanov, A. N. & Panagopoulos, C. Physical foundations and basic properties of magnetic skyrmions. *Nat. Rev. Phys.* **2**, 492–498 (2020).
12. Tokura, Y. & Kanazawa, N. Magnetic skyrmion materials. *Chem. Rev.* **121**, 2857–2897 (2021).
13. Seki, S., Yu, X. Z., Ishiwata, S. & Tokura, Y. Observation of skyrmions in a multiferroic material. *Science* **336**, 198–201 (2012).
14. Ruff, E. et al. Multiferroicity and skyrmions carrying electric polarization $InGaV_4S_8$. *Sci. Adv.* **1**, e1500916 (2015).
15. Okamura, Y., Kagawa, F., Seki, S. & Tokura, Y. Transition to and from the skyrmion lattice phase by electric fields in a magnetoelectric compound. *Nat. Commun.* **7**, 12669 (2016).
16. Hsu, Pin-Jui et al. Electric-field-driven switching of individual magnetic skyrmions. *Nat. Nanotechnol.* **12**, 123–126 (2017).
17. Behera, A. K., Chowdhury, S. & Das, S. R. Magnetic skyrmions in atomic thin CrI3 monolayer. *Appl. Phys. Lett.* **114**, 232402 (2019).
18. Desplat, L. et al. Mechanism for ultrafast electric-field-driven skyrmion nucleation. *Phys. Rev. B* **104**, L060409 (2021).
19. Jingman, P. et al. Electric-field-induced formation and annihilation of skyrmions in a two-dimensional magnet. *Phys. Rev. B* **108**, 134430 (2023).
20. Chaudron, A. et al. Electric-field-induced multiferroic topological solitons, *Nat. Mater*. https://doi.org/10.1038/s41563-024-01890-4 (2024).
21. Bayaraa, T., Xu, C., Yang, Y., Xiang, H. & Bellaiche, L. Magnetic-domain-wall-induced electrical polarization in rare-earth iron garnet systems: A first-principles study. *Phys. Rev. Lett.* **125**, 067602 (2020).
22. Yang, Y. et al. Improper ferroelectricity at antiferromagnetic domain walls of perovskite oxides. *Phys. Rev. B* **96**, 104431 (2017).
23. Wang, W., Sun, W., Zhang, G., Cheng, Z. & Wang, Y. Magnetic domain-wall induced ferroelectric polarization in rare-earth orthoferrites afeo3 (a = lu, y, gd):first-principles calculations. *J. Mater. Chem. C.* **7**, 10059–10065 (2019).
24. Zhou, HaiYang, Zhao, HongJian, Zhang, WenQing & Chen, XiangMing Magnetic domain wall induced ferroelectricity in double perovskites. *Appl. Phys. Lett.* **106**, 152901 (2015).
25. Ghosh, S., Stojić, N. & Binggeli, N. Comment on "Magnetic skyrmions in atomic thin CrI3 monolayer" [Appl. Phys. Lett. 114, 232402 (2019)]. *Appl. Phys. Lett.* **116**, 086101 (2020).
26. Vishkayi, S., Torbatian, Z., Qaiumzadeh, A. & Asgari, R. Strain and electric-field control of spin-spin interactions in monolayer CrI_3. *Phys. Rev. Mater.* **4**, 094004 (2020).
27. Huang, B. et al. Layer-dependent ferromagnetism in a van der Waals crystal down to the monolayer limit. *Nature* **546**, 270–273 (2017).

28. Gong, C. et al. Discovery of intrinsic ferromagnetism in two-dimensional van der Waals crystals. *Nature* **546**, 265–269 (2017).
29. McGuire, M. A. Crystal and magnetic structures in layered, transition metal dihalides and trihalides. *Crystals* **7**, 121 (2017).
30. Burch, K. S., Mandrus, D. & Park, Je-Geun Magnetism intwo-dimensional van der waals materials. *Nature* **563**, 47–52 (2018).
31. Song, Q. et al. Evidence for a single-layer van der multiferroic. *Nature* **602**, 601–605 (2022).
32. Han, Myung-Geun et al. Topological magnetic-spin textures in two-dimensional vander Waals $Cr_2Ge_2Te_6$. *Nano Lett.* **19**, 7859–7865 (2019).
33. Zubko, P., Catalan, G. & Tagantsev, A. K. Flexoelectric effect in solids. *Annu. Rev. Mater. Res.* **43**, 387–421 (2013).
34. Springolo, M., Royo, M. & Stengel, M. Direct and converse flexoelectricity in two-dimensional materials. *Phys. Rev. Lett.* **127**, 216801 (2021).
35. Springolo, M., Royo, M. & Stengel, M. In-planeflexoelectricity in two-dimensional D_{3d} crystals. *Phys. Rev. Lett.* **131**, 236203 (2023).
36. Hertel, R. Curvature-induced magnetochirality. *SPIN* **03**, 1340009 (2013).
37. Edström, A., Amoroso, D., Picozzi, S., Barone, P. & Stengel, M. Curved magnetism in cri_3. *Phys. Rev. Lett.* **128**, 177202 (2022).
38. Sheka, D. D., Kravchuk, V. P. & Gaididei, Y. Curvature effects in statics and dynamics of low-dimensional magnets. *J. Phys. A: Math. Theor.* **48**, 125202 (2015).
39. Streubel, R. et al. Magnetism in curved geometries. *J. Phys. D: Appl. Phys.* **49**, 363001 (2016).
40. Sheka, D. D. A perspective on curvilinear magnetism. *Appl. Phys. Lett.* **118**, 230502 (2021).
41. Dzyaloshinsky, I. A thermodynamic theory of weak ferromagnetism of antiferromagnetics. *J. Phys. Chem. Solids* **4**, 241–255 (1958).
42. Moriya, T. Anisotropic superexchange interaction and weak ferromagnetism. *Phys. Rev.* **120**, 91–98 (1960).
43. Mostovoy, M. Ferroelectricity in spiral magnets. *Phys. Rev. Lett.* **96**, 067601 (2006).
44. Katsura, H., Nagaosa, N. & Balatsky, A. V. Spin current and magnetoelectric effect in noncollinear magnets. *Phys. Rev. Lett.* **95**, 057205 (2005).
45. Seki, S., Onose, Y. & Tokura, Y. Spin-driven ferroelectricity in triangular lattice antiferromagnets $ACrO_2$ (A=Cu, Ag, Li, or Na). *Phys. Rev. Lett.* **101**, 067204 (2008).
46. Kaplan, T. A. & Mahanti, S. D. Canted-spin-caused electric dipoles: A local symmetry theory. *Phys. Rev. B* **83**, 174432 (2011).
47. Xiang, H. J., Kan, E. J., Zhang, Y., Whangbo, M.-H. & Gong, X. G. General theory for the ferroelectric polarization induced by spin-spiral order. *Phys. Rev. Lett.* **107**, 157202 (2011).
48. Yang, J. H. et al. Strong Dzyaloshinskii-Moriya interaction and origin of ferroelectricity in Cu_2OSeO_3. *Phys. Rev. Lett.* **109**, 107203 (2012).
49. Lu, X. Z., Whangbo, M.-H., Dong, S., Gong, X. G. & Xiang, H. J. Giant ferroelectric polarization of $CaMn_7O_{12}$ induced by a combined effect of Dzyaloshinskii-Moriya interaction and exchange striction. *Phys. Rev. Lett.* **108**, 187204 (2012).
50. Hwang, J. et al. Successive magnetic phase transitions and multiferroicity in the spin-one triangular-lattice antiferromagnet $Ba_3NiB_2O_9$. *Phys. Rev. Lett.* **109**, 257205 (2012).
51. Sharma, G., Saha, J., Kaushik, S. D., Siruguri, V. & Patnaik, S. Improper ferroelectricity in helicoidal antiferromagnet $Cu_3Nb_2O_8$. *Solid State Commun.* **203**, 54–57 (2015).
52. Chai, Y., Chun, S., Cong, J. & Kim, K. Magnetoelectricity in multiferroic hexaferrites as understood by crystal symmetry analyses. *Phys. Rev. B* **98**, 104416 (2018).
53. Tang, Y. S. et al. Metamagnetic transitions and magnetoelectricity in the spin-1 honeycomb antiferromagnet $Ni_2Mo_3O_8$. *Phys. Rev. B* **103**, 014112 (2021).
54. Xiang, H. J., Wang, P. S., Whangbo, M.-H. & Gong, X. G. Unified model of ferroelectricity induced by spin order. *Phys. Rev. B* **88**, 054404 (2013).
55. Stengel, M. Macroscopic polarization from nonlinear gradient couplings. *Phys. Rev. Lett.* **132**, 146801 (2024).
56. Grytsiuk, S. et al. Ab initio analysis of magnetic properties of the prototypeb20 chiral magnet FeGe. *Phys. Rev. B* **100**, 214406 (2019).
57. Kvashnin, Y. O., Bergman, A., Lichtenstein, A. I. & Katsnelson, M. I. Relativistic exchange interactions in CrX_3 (x=Cl, Br, I) monolayers. *Phys. Rev. B* **102**, 115162 (2020).
58. Chen, L. et al. Topological spin excitations in honeycomb ferromagnet CrI_3. *Phys. Rev. X* **8**, 041028 (2018).
59. Liu, J., Shi, M., Lu, J. & Anantram, M. P. Analysis of electrical-field-dependent Dzyaloshinskii-Moriya interaction and magnetocrystalline anisotropy in a two-dimensional ferromagnetic monolayer. *Phys. Rev. B* **97**, 054416 (2018).
60. Eriksson, O., Bergman, A., Bergqvist, L. & Hellsvik, J. *Atomistic Spin Dynamics: Foundations* ://www.oxfordscholarship.com/10.1093/oso/9780198788669.001.0001/oso-9780198788669 (Oxford University Press, Oxford, 2017).
61. Ressouche, E., Loire, M., Simonet, V., Ballou, R., Stunault, A. & Wildes, A. Magnetoelectric $MnPS_3$ as a candidate for ferrotoroidicity. *Phys. Rev. B* **82**, 100408 (2010).
62. Kimura, T., Lashley, J. C. & Ramirez, A. P. Inversion-symmetry breaking in the noncollinear magnetic phase of the triangular-lattice antiferromagnetic $CuFeO_2$. *Phys. Rev. B* **73**, 220401 (2006).
63. Liu, C., Ren, W. & Picozzi, S. Spin-chirality-driven multiferroicity in van der Waals monolayers. *Phys. Rev. Lett.* **132**, 086802 (2024).
64. Prokhnenko, O. et al. Enhanced ferroelectric polarization by induceddy spin order in multiferroic $DyMnO_3$. *Phys. Rev. Lett.* **98**, 057206 (2007).
65. Picozzi, S., Yamauchi, K., Sanyal, B., Sergienko, I. A. & Dagotto, E. Dual nature of improper ferroelectricity in amagnetoelectric multiferroic. *Phys. Rev. Lett.* **99**, 227201 (2007).
66. Picozzi, S. & Ederer, C. First principles studies of multiferroic materials. *J. Phys.: Condens. Matter* **21**, 303201 (2009).
67. Abdul-Wahab, D. et al. Domain wall dynamics in two-dimensional van der waals ferromagnets. *Appl. Phys. Rev.* **8**, 041411 (2021).
68. Wahab, D. A. et al. Quantum rescaling, domain metastability, and hybrid domain-walls in 2D Cri3 magnets, *Adv. Mater.* **33**, 2004138.
69. Fujita, R. et al. Layer-dependent magnetic domains in atomically thin Fe_5GeTe_2. *ACSNano* **16**, 10545–10553 (2022).
70. Sun, Qi-Chao et al. Magnetic domains and domain wall pinning in atomically thin CrBr3 revealed by nanoscale imaging. *Nat. Commun.* **12**, 1989 (2021).
71. Zhang, G. et al. Field-free room-temperature modulation of magnetic bubble and stripedomains in 2D van der Waals ferromagnetic Fe_3GaTe_2. *Appl. Phys. Lett.* **123**, 101901 (2023).
72. Kittel, C. Theory of the structure of ferromagnetic domains in films and small particles. *Phys. Rev.* **70**, 965–971 (1946).
73. Knüpfer, H., Muratov, C. B. & Nolte, F. Magnetic domains in thin ferromagnetic films with strong perpendicular anisotropy. *Arch. Ration. Mech. Anal.* **232**, 727–761 (2019).
74. Nikolaev, S. A. & Solovyev, I. V. Microscopic theory of electric polarization induced by skyrmionic order $InGaV_4S_8$. *Phys. Rev. B* **99**, 100401 (2019).
75. Göbel, B. örge, Mertig, I. & Tretiakov, O. A. Beyondskyrmions: Review and perspectives of alternative magnetic quasiparticles. *Phys. Rep.* **895**, 1–28 (2021).
76. Junquera, J. et al. Topological phases in polar oxide nanostructures. *Rev. Mod. Phys.* **95**, 025001 (2023).
77. Rohart, S., Miltat, J. & Thiaville, A. Path to collapse for an isolated néel skyrmion. *Phys. Rev. B* **93**, 214412 (2016).

78. Lobanov, I. S., Jónsson, H. & Uzdin, V. M. Mechanism and activation energy of magnetic skyrmion annihilation obtained from minimum energy path calculations. *Phys. Rev. B* **94**, 174418 (2016).
79. Murakawa, H., Onose, Y., Miyahara, S., Furukawa, N. & Tokura, Y. Ferroelectricity induced by spin-dependent metal-ligand hybridization in $Ba2CoGe_2O_7$. *Phys. Rev. Lett.* **105**, 137202 (2010).
80. Yamauchi, K., Barone, P. & Picozzi, S. Theoretical investigation of magnetoelectric effects in$ba_2coge_2o_7$. *Phys. Rev. B* **84**, 165137 (2011).
81. Barone, P., Yamauchi, K. & Picozzi, S. Ferroelectricity due to orbital ordering in *e*-type undoped rare-earth manganites. *Phys. Rev. Lett.* **106**, 077201 (2011).
82. Szilva, A. et al. Quantitative theory of magnetic interactions in solids. *Rev. Mod. Phys.* **95**, 035004 (2023).
83. Blöchl, P. E. Projector augmented-wave method. *Phys. Rev. B* **50**, 17953–17979 (1994).
84. Kresse, G. & Joubert, D. From ultrasoft pseudopotentials to the projector augmented-wave method. *Phys. Rev. B* **59**, 1758–1775 (1999).
85. Kresse, G. & Furthmüller, J. Efficiency of ab-initio total energy calculations for metals and semiconductors using a plane-wave basis set. *Comput. Mater. Sci.* **6**, 15 – 50 (1996).
86. Kresse, G. & Hafner, J. Ab initio molecular-dynamics simulation of the liquid-metal-amorphous semiconductortransition in germanium. *Phys. Rev. B* **49**, 14251–14269 (1994).
87. Kresse, G. & Hafner, J. Ab initio molecular dynamics for liquid metals. *Phys. Rev. B* **47**, 558–561 (1993).
88. Xu, C., Feng, J., Xiang, H. & Bellaiche, L. Interplay between Kitaev interaction and single ion anisotropy in ferromagnetic CrI_3 and $CrGeTe_3$ monolayers. *npj Comput. Mater.* **4**, 57 (2018).
89. Dudarev, S. L., Botton, G. A., Savrasov, S. Y., Humphreys, C. J. & Sutton, A. P. Electron-energy-loss spectra and the structural stability of nickel oxide: An LSDA+U study. *Phys. Rev. B* **57**, 1505–1509 (1998).
90. Lado, J. L. & Fernández-Rossier, J. On the origin of magnetic anisotropy in two-dimensional CrI_3. *2D Mater.* **4**, 035002 (2017).
91. Besbes, O., Nikolaev, S., Meskini, N. & Solovyev, I. Microscopic origin of ferromagnetism in the trihalides $CrCl_3$ and CrI_3. *Phys. Rev. B* **99**, 104432 (2019).
92. Perdew, J. P., Burke, K. & Ernzerhof, M. Generalized gradient approximation made simple. *Phys. Rev. Lett.* **77**, 3865–3868 (1996).
93. Hobbs, D., Kresse, G. & Hafner, J. Fully unconstrained noncollinear magnetism within the projector augmented-wave method. *Phys. Rev. B* **62**, 11556–11570 (2000).
94. Ma, Pui-Wai & Dudarev, S. L. Constrained density functional for noncollinear magnetism. *Phys. Rev. B* **91**, 054420 (2015).
95. King-Smith, R. D. & Vanderbilt, D. Theory of polarization of crystalline solids. *Phys. Rev. B* **47**, 1651–1654 (1993).
96. Royo, M. & Stengel, M. Exact long-range dielectric screening and interatomic force constants in quasi-two-dimensional crystals. *Phys. Rev. X* **11**, 041027 (2021).
97. Ismail-Beigi, S. Truncation of periodic image interactions for confined systems. *Phys. Rev. B* **73**, 233103 (2006).
98. Rozzi, C. A., Varsano, D., Marini, A., Gross, E. K. U. & Rubio, A. Exact Coulomb cutoff technique for supercell calculations. *Phys. Rev. B* **73**, 205119 (2006).
99. Sohier, T., Calandra, M. & Mauri, F. Density functional perturbation theory for gated two-dimensional heterostructures: Theoretical developments and application to flexural phonons in graphene. *Phys. Rev. B* **96**, 075448 (2017).

Acknowledgements

A.E. acknowledges insightful discussions with F. N. Rybakov, and financial support from the Swedish Research Council (VR - 2018-06807 and 2022-04720), ÅForsk (22-441), the Göran Gustafsson Foundation, and the Swedish e-Science Research Center (SeRC). M.S. acknowledges the support of the State Investigation Agency through the Severo Ochoa Program for Centres of Excellence in R&D (CEX2023-001263-S), of the Ministry of Science, Innovation and Universities (Grant No. PID2023-152710NB-I00) and of Generalitat de Catalunya (Grant No. 2021 SGR 01519). This work has been funded by the European Union - NextGenerationEU, under the Italian Ministry of University and Research (MUR) PRIN-2022 project "SORBET: Spin-ORBit Effects in Two-dimensional magnets" (IT-MIUR Grant No. 2022ZY8HJY) and National Innovation Ecosystem grant ECS00000041 - VITALITY - CUP B43C22000470005. Computational work was done on resources at PDC, Stockholm, and NSC, Linköping, via the National Academic Infrastructure for Supercomputing in Sweden (NAISS), as well as the Galileo system of Cineca through HPC-Europa3 (HPC17A3WLE), which also supported the collaborative effort by funding an international research visit.

Author contributions

All authors contributed to the extensive scientific discussion from the start to finalizing the project. All authors contributed to writing the manuscript and revised and approved the final version. A.E. performed all calculations and drafted the manuscript. P.B. performed the symmetry analysis of the atomistic model.

Funding

Open access funding provided by Royal Institute of Technology.

Competing interests

The authors declare no competing interests.

Additional information

Supplementary information The online version contains supplementary material available at https://doi.org/10.1038/s41524-025-01795-z.

Correspondence and requests for materials should be addressed to Alexander Edström or Paolo Barone.